

Distributed parameter and finite element models for wave propagation in railway contact lines

Original

Distributed parameter and finite element models for wave propagation in railway contact lines / Sorrentino, S.; Anastasio, D.; Fasana, A.; Marchesiello, S.. - In: JOURNAL OF SOUND AND VIBRATION. - ISSN 0022-460X. - STAMPA. - 410:(2017), pp. 1-18. [10.1016/j.jsv.2017.08.008]

Availability:

This version is available at: 11583/2695223 since: 2020-07-09T12:09:38Z

Publisher:

Elsevier

Published

DOI:10.1016/j.jsv.2017.08.008

Terms of use:

This article is made available under terms and conditions as specified in the corresponding bibliographic description in the repository

Publisher copyright

(Article begins on next page)



Distributed parameter and finite element models for wave propagation in railway contact lines

S. Sorrentino¹, D. Anastasio², A. Fasana² and S. Marchesiello^{2,*}

¹*Dipartimento di Ingegneria Enzo Ferrari, Università di Modena e Reggio Emilia, Via Vivarelli 10, 41125 Modena, Italy.*

²*Dipartimento di Ingegneria Meccanica ed Aerospaziale, Politecnico di Torino, Corso Duca degli Abruzzi 24, 10129 Torino, Italy.*

<https://doi.org/10.1016/j.jsv.2017.08.008>

Cite as:

S. Sorrentino, D. Anastasio, A. Fasana, S. Marchesiello, Distributed parameter and finite element models for wave propagation in railway contact lines, J. Sound Vib. 410 (2017) 1-18.

DISTRIBUTED PARAMETER AND FINITE ELEMENT MODELS FOR WAVE PROPAGATION IN RAILWAY CONTACT LINES

S. Sorrentino¹, D. Anastasio², A. Fasana² and S. Marchesiello^{2,*}

¹Dipartimento di Ingegneria Enzo Ferrari

Università di Modena e Reggio Emilia

Via Vivarelli 10

41125 Modena, ITALY

²Dipartimento di Ingegneria Meccanica e Aerospaziale,

Politecnico di Torino,

Corso Duca degli Abruzzi 24

10129 Torino, ITALY

ABSTRACT

A distributed parameter model of a railway two-level catenary system is presented for the analysis of the coupled wave dynamics. The wires are modelled as two straight axis parallel beams, with linear equilibrium equations, and the moving load applied by the pantograph is modelled as a constant concentrated travelling force. The general solution is sought by an application of the Ritz–Galerkin method, and then compared with direct time integrations of a finite element model (FEM), achieved by two different integration schemes. The proposed model provides a valid reference for appropriately selecting the FEM parameters, in order to reduce the errors due to spurious modes, affecting the numerical integrations especially at high speeds of the moving pantograph.

** Corresponding author. Tel.: +390110906947; fax: +390110906999; e-mail address: stefano.marchesiello@polito.it*

Keywords

Overhead contact lines; moving loads; distributed parameter model; wave propagation; finite element model.

1. Introduction

Railway catenary systems, supplying trains with electric power, play an important role in determining the maximum allowable railway velocity, which is limited to a certain percentage of the wave propagation velocity of the contact wire. The analysis of their dynamic behaviour is not straightforward, basically consisting of a wave propagation problem in structures excited by moving loads [1], and the bibliography on the specific topic is not extensive.

In [2] an analytical method is proposed for calculating the steady-state response of a two-level catenary to a moving pantograph, represented by a travelling constant force; the model for the catenary consists of two strings, the upper one fixed at periodically spaced points, connected each other by equidistant lumped mass-spring-dashpot elements. In [3] it is recognized that a beam model with dispersive wave characteristics better represents the contact wire than a string model, and a method is presented in the paper for estimating the wave propagation velocity of a railway contact wire by applying a wavelet transform to experimental signals. The problem of flexural oscillations of a single infinite beam resting on identical periodic simple elastic supports, caused by a harmonic concentrated force moving steadily along the beam, is solved in [4] with an application of the Fourier transform. Using modal analysis, the deflection of a single beam of finite length without intermediate supports, subjected to an axial tensile force and a moving concentrated force, has been analytically determined in [5].

A two-level catenary including bending stiffness in the wires has been considered in [6], expressing the displacements as finite sums of sine functions, and computing the responses of the discretized system via Lagrange equation's method. The same approach has been adopted also in [7], with additional inclusion in the numerical model of a three degrees of freedom pantograph with unilateral contact.

In this study a distributed parameter model of a railway two-level catenary system is presented for the analysis of the coupled wave dynamics. The contact and messenger wires are modelled as two straight axis Euler–Bernoulli parallel beams, while the moving load applied by the pantograph is represented by a constant travelling force. The wires are interconnected by non-equally spaced linearly elastic droppers with lumped masses, and supported by linearly elastic brackets. The contact wire holds lumped masses positioned in correspondence of each bracket and representing the registration arms. The general solution is sought by the Ritz–Galerkin method, using a set of comparison functions [8] given by the eigenfunctions of a pinned–pinned Euler–Bernoulli beam.

The results of the presented method are given providing complete analytical developments and are compared with direct time integrations of a FEM of the system, which is the common approach to solve the problem under analysis [9–10], for its high flexibility and relatively easy implementation.

Unfortunately, the complexity of the dynamic behaviour may cause numerical errors affecting the FEM solutions, especially at high speeds of the moving pantograph. These errors are very often related to numerical wave modes, or spurious modes, introduced by the time integration algorithms.

The most common technique to discard spurious modes consists in adding numerical damping, either by an intrinsic property of the algorithm, as in the Bathe method [11], or by using explicit parameters, as in the Generalized- α method [12]. Both methods are compared with the proposed distributed parameter technique.

2. Distributed parameter model

A distributed parameter model of a railway catenary system is considered, with some simplifying assumptions: the wires are modelled as two straight axis parallel beams, with linear equilibrium equations (neglecting in particular the slackening of the droppers), while the moving load applied by the pantograph is simply modelled as a constant concentrated travelling force. Damp-

ing is disregarded in the model under investigation, because it is often considered as negligible (as suggested by [13]). Moreover, one of the main purposes of the paper is to discuss the numerical damping added by integration algorithms and this effect can be better highlighted for undamped systems. Introducing damping phenomena carries further analytical and computational effort, in particular when non-proportional damping distribution is taken into account [14-17].

2.1. Description of the model

The model consists of two parallel pinned–pinned Euler–Bernoulli beams (representing the contact wire and the messenger wire), interconnected by H linearly elastic droppers with lumped masses, and supported by J linearly elastic brackets. In addition, the contact wire holds J lumped masses representing the registration arms, positioned in correspondence of a bracket as shown in Fig. 1. The adopted nomenclature is reported in Appendix A.

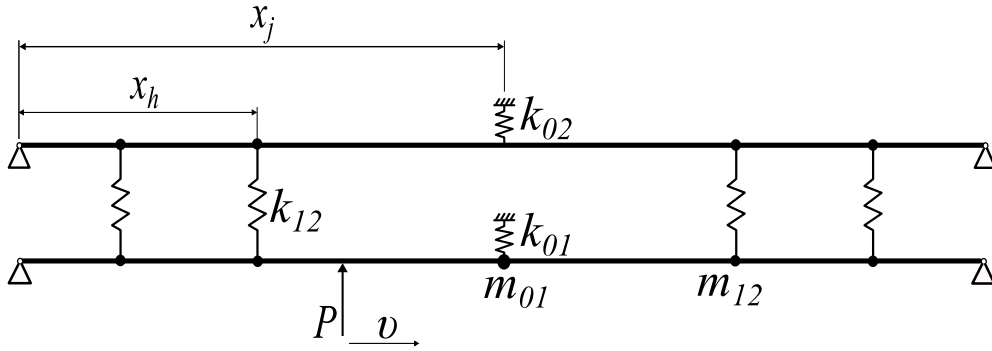


Fig. 1. Schematic of the distributed parameter model.

The two coupled equilibrium equations, one for the contact wire (subscript 1) and the other for the messenger wire (subscript 2), can be written in the form:

$$\begin{cases} \mu_1 \frac{\partial^2 w_1}{\partial t^2} + K_1 \frac{\partial^4 w_1}{\partial x^4} - T_1 \frac{\partial^2 w_1}{\partial x^2} + \left[m_{01} \frac{\partial^2 w_1}{\partial t^2} + k_{01} w_1 \right] \sum_{j=1}^J \delta(x - x_j) + \left[m_{12} \frac{\partial^2 w_1}{\partial t^2} + k_{12} (w_1 - w_2) \right] \sum_{h=1}^H \delta(x - x_h) = f(x, t) \\ \mu_2 \frac{\partial^2 w_2}{\partial t^2} + K_2 \frac{\partial^4 w_2}{\partial x^4} - T_2 \frac{\partial^2 w_2}{\partial x^2} + k_{02} w_2 \sum_{j=1}^J \delta(x - x_j) + \left[m_{12} \frac{\partial^2 w_2}{\partial t^2} + k_{12} (w_2 - w_1) \right] \sum_{h=1}^H \delta(x - x_h) = 0 \end{cases} \quad (1)$$

where $\delta(\cdot)$ is the Dirac distribution and $f(x, t)$ represents an external force density acting on the contact wire.

2.2. Solution for a travelling constant force

For a constant load travelling at a speed v , the external force density acting on the contact wire

can be expressed as

$$f(x, t) = \begin{cases} P\delta(x - vt), & 0 \leq t \leq t_e, \\ 0, & t > t_e \end{cases}, \quad t_e = \frac{L}{v} \quad (2)$$

The solution is sought by the Ritz–Galerkin method, using a set of N comparison functions [8] given by the first N eigenfunctions of a pinned–pinned Euler–Bernoulli beam of length L :

$$\mathbf{\Phi} = \{\phi_n(x)\}_{N \times 1}, \quad \phi_n(x) = \sin\left(\frac{n\pi x}{L}\right), \quad n = 1 \dots N \Rightarrow \begin{cases} w_1(x, t) = \mathbf{\Phi}^T \mathbf{\eta}_1, & \mathbf{\eta}_1 = \{\eta_{1n}(t)\}_{N \times 1} \\ w_2(x, t) = \mathbf{\Phi}^T \mathbf{\eta}_2, & \mathbf{\eta}_2 = \{\eta_{2n}(t)\}_{N \times 1} \end{cases} \quad (3)$$

After introducing the expressions of w_1 and w_2 , eqs. (3), in the equilibrium equations (1), the latter are multiplied by $\mathbf{\Phi}$ and then integrated over the entire spatial domain, yielding a mass matrix \mathbf{M} and a stiffness matrix \mathbf{K} in the form:

$$\begin{aligned} \mathbf{M} &= \frac{1}{2}L \begin{bmatrix} \mu_1 \mathbf{I} & \mathbf{0} \\ \mathbf{0} & \mu_2 \mathbf{I} \end{bmatrix} + \begin{bmatrix} m_{01} \mathbf{\Sigma}_J & \mathbf{0} \\ \mathbf{0} & \mathbf{0} \end{bmatrix} + m_{12} \begin{bmatrix} \mathbf{\Sigma}_H & \mathbf{0} \\ \mathbf{0} & \mathbf{\Sigma}_H \end{bmatrix} \\ \mathbf{K} &= \frac{1}{2}L \begin{bmatrix} \mathbf{D}_1 & \mathbf{0} \\ \mathbf{0} & \mathbf{D}_2 \end{bmatrix} + \begin{bmatrix} k_{01} \mathbf{\Sigma}_J & \mathbf{0} \\ \mathbf{0} & k_{02} \mathbf{\Sigma}_J \end{bmatrix} + k_{12} \begin{bmatrix} \mathbf{\Sigma}_H & -\mathbf{\Sigma}_H \\ -\mathbf{\Sigma}_H & \mathbf{\Sigma}_H \end{bmatrix} \end{aligned} \quad (4)$$

where both \mathbf{M} and \mathbf{K} are $2N \times 2N$ matrices, while the $N \times N$ inner matrices are:

$$\begin{aligned} \mathbf{I} &= \text{diag}\{1\}, \quad \mathbf{0} = \text{diag}\{0\}, \\ \mathbf{\Sigma}_J &= \sum_{j=1}^J \{\phi_n(x_j)\} \{\phi_n(x_j)\}^T, \quad \mathbf{\Sigma}_H = \sum_{h=1}^H \{\phi_n(x_h)\} \{\phi_n(x_h)\}^T, \\ \mathbf{D}_1 &= \text{diag} \left\{ \left(\frac{n\pi}{L} \right)^2 \left[T_1 + \left(\frac{n\pi}{L} \right)^2 K_1 \right] \right\}, \quad \mathbf{D}_2 = \text{diag} \left\{ \left(\frac{n\pi}{L} \right)^2 \left[T_2 + \left(\frac{n\pi}{L} \right)^2 K_2 \right] \right\} \end{aligned} \quad (5)$$

The solution of the algebraic eigenproblem:

$$[\mathbf{K} - \omega^2 \mathbf{M}] \mathbf{z} = \mathbf{0} \quad (6)$$

yields a set of $2N$ natural angular frequencies ω_n and a set of $2N$ real eigenvectors \mathbf{z}_n . These natural angular frequencies may be compared with those of the two beams without intermediate elastic constraints and lumped masses (say ω_{1n} and ω_{2n}):

$$\omega_{1n} = \frac{n\pi}{L} \sqrt{\frac{T_1}{\mu_1} + \left(\frac{n\pi}{L} \right)^2 \frac{K_1}{\mu_1}}, \quad \omega_{2n} = \frac{n\pi}{L} \sqrt{\frac{T_2}{\mu_2} + \left(\frac{n\pi}{L} \right)^2 \frac{K_2}{\mu_2}} \quad (7)$$

After partitioning the n^{th} eigenvector in two vectors of size N (components of \mathbf{z}_n from 1 to N , and from $N+1$ to $2N$ respectively):

$$\mathbf{z}_n = \begin{bmatrix} \boldsymbol{\Psi}_n \\ \boldsymbol{\zeta}_n \end{bmatrix} \quad (8)$$

the general integral can be expressed in the form:

$$\begin{cases} w_{1g}(x, t) = \sum_{n=1}^{2N} \left\{ \boldsymbol{\Phi}^T \boldsymbol{\Psi}_n [A_n \cos(\omega_n t) + B_n \sin(\omega_n t)] \right\} \\ w_{2g}(x, t) = \sum_{n=1}^{2N} \left\{ \boldsymbol{\Phi}^T \boldsymbol{\zeta}_n [A_n \cos(\omega_n t) + B_n \sin(\omega_n t)] \right\} \end{cases} \quad (9)$$

where the spatial coordinate x is hidden in the vector $\boldsymbol{\Phi}$, while A_n and B_n are constants depending on the initial conditions.

The particular integral can be found by writing the equation of motion according to eqs. (4):

$$\mathbf{M}\ddot{\boldsymbol{\eta}} + \mathbf{K}\boldsymbol{\eta} = \mathbf{f}, \quad \boldsymbol{\eta} = \begin{bmatrix} \boldsymbol{\eta}_1 \\ \boldsymbol{\eta}_2 \end{bmatrix} = \sum_{n=1}^{2N} \mathbf{z}_n p_n(t), \quad \mathbf{f} = P \begin{bmatrix} \boldsymbol{\Phi}(vt) \\ \mathbf{0} \end{bmatrix} \quad (10)$$

Introducing now an angular frequency ω_0 , given by the pantograph travelling at a constant speed v :

$$\omega_0 = \frac{\pi v}{L} \quad (11)$$

eqs. (10) can be decoupled and solved in the form:

$$\ddot{p}_n(t) + \omega_n^2 p_n(t) = \frac{P}{m_n} \sum_{r=1}^N \psi_{nr} \sin(r\omega_0 t) \Rightarrow p_n(t) = \frac{P}{m_n} \sum_{r=1}^N \frac{\psi_{nr}}{\omega_n^2 - (r\omega_0)^2} \sin(r\omega_0 t) \quad (12)$$

where m_n represents the n^{th} modal mass of the system. In the particular case in which both $\mu_1 = \mu_2 = \mu$ and $m_{01} = m_{12} = 0$, then:

$$m_n = \frac{1}{2} \mu L \quad \forall n \quad (13)$$

Recalling eqs. (3), (8) and (10), the particular integral can be obtained directly from eqs. (12):

$$\begin{cases} w_{1p}(x, t) = P \sum_{n=1}^{2N} \left\{ \frac{\boldsymbol{\Phi}^T \boldsymbol{\Psi}_n}{m_n} \sum_{r=1}^N \frac{\psi_{nr}}{\omega_n^2 - (r\omega_0)^2} \sin(r\omega_0 t) \right\} \\ w_{2p}(x, t) = P \sum_{n=1}^{2N} \left\{ \frac{\boldsymbol{\Phi}^T \boldsymbol{\zeta}_n}{m_n} \sum_{r=1}^N \frac{\psi_{nr}}{\omega_n^2 - (r\omega_0)^2} \sin(r\omega_0 t) \right\} \end{cases} \quad (14)$$

Adding the general integral w_g eqs. (9) to the particular integral w_p eqs. (14), and introducing the initial conditions (zero displacement and zero velocity):

$$\begin{cases} w_1(x, 0) = w_2(x, 0) = 0 \quad \forall x \in [0, L] \\ \dot{w}_1(x, 0) = \dot{w}_2(x, 0) = 0 \quad \forall x \in [0, L] \end{cases} \Rightarrow A_n = 0, \quad B_n = -P \sum_{r=1}^N \frac{r\omega_0}{m_n \omega_n} \left[\frac{\psi_{nr}}{\omega_n^2 - (r\omega_0)^2} \right] \quad (15)$$

yield the solution for $0 \leq t \leq t_e$ in the form:

$$\begin{cases} w_1(x, t) = P \sum_{n=1}^{2N} \left\{ \frac{\Phi^T \Psi_n}{m_n} \left[\sum_{r=1}^N \frac{\psi_{nr}}{\omega_n^2 - (r\omega_0)^2} \left(\sin(r\omega_0 t) - \frac{r\omega_0}{\omega_n} \sin(\omega_n t) \right) \right] \right\} \\ w_2(x, t) = P \sum_{n=1}^{2N} \left\{ \frac{\Phi^T \zeta_n}{m_n} \left[\sum_{r=1}^N \frac{\psi_{nr}}{\omega_n^2 - (r\omega_0)^2} \left(\sin(r\omega_0 t) - \frac{r\omega_0}{\omega_n} \sin(\omega_n t) \right) \right] \right\} \end{cases} \quad (16)$$

or alternatively, with the spatial variable appearing explicitly:

$$\begin{cases} w_1(x, t) = P \sum_{n=1}^{2N} \frac{1}{m_n} \left\{ \left[\sum_{r=1}^N \psi_{nr} \sin\left(\frac{r\pi x}{L}\right) \right] \left[\sum_{r=1}^N \psi_{nr} \frac{1}{\omega_n^2 - (r\omega_0)^2} \left(\sin(r\omega_0 t) - \frac{r\omega_0}{\omega_n} \sin(\omega_n t) \right) \right] \right\} \\ w_2(x, t) = P \sum_{n=1}^{2N} \frac{1}{m_n} \left\{ \left[\sum_{r=1}^N \zeta_{nr} \sin\left(\frac{r\pi x}{L}\right) \right] \left[\sum_{r=1}^N \psi_{nr} \frac{1}{\omega_n^2 - (r\omega_0)^2} \left(\sin(r\omega_0 t) - \frac{r\omega_0}{\omega_n} \sin(\omega_n t) \right) \right] \right\} \end{cases} \quad (17)$$

Adopting mass-normalized eigenvectors, i.e.:

$$\hat{\mathbf{z}}_n = \begin{bmatrix} \hat{\Psi}_n \\ \hat{\zeta}_n \end{bmatrix} = \frac{1}{\sqrt{m_n}} \mathbf{z}_n = \frac{1}{\sqrt{m_n}} \begin{bmatrix} \Psi_n \\ \zeta_n \end{bmatrix} \quad (18)$$

the notation in eqs. (17) would be simplified with $m_n = 1$. Note that the only distinction between w_1 and w_2 is a different factor ($\psi_{nr} \leftrightarrow \zeta_{nr}$) in the first square brackets.

For $t > t_e$ the solution is a free response that can be expressed by means of the general integral eqs. (9) alone, with initial conditions given by:

$$\begin{cases} w_1(x, t_e), & w_2(x, t_e) \\ \dot{w}_1(x, t_e), & \dot{w}_2(x, t_e) \end{cases} \quad (19)$$

which can be computed from eqs. (17) at $t = t_e$. After some passages the free response can be written as:

$$\begin{cases} w_1(x, t) = P \sum_{n=1}^{2N} \frac{1}{m_n} \left\{ \left[\sum_{r=1}^N \psi_{nr} \sin\left(\frac{r\pi x}{L}\right) \right] \left[\sum_{r=1}^N \psi_{nr} \frac{1}{\omega_n^2 - (r\omega_0)^2} \left(\frac{r\omega_0}{\omega_n} \right) \left[(-1)^r \sin[\omega_n(t - t_e)] - \sin(\omega_n t) \right] \right] \right\} \\ w_2(x, t) = P \sum_{n=1}^{2N} \frac{1}{m_n} \left\{ \left[\sum_{r=1}^N \zeta_{nr} \sin\left(\frac{r\pi x}{L}\right) \right] \left[\sum_{r=1}^N \psi_{nr} \frac{1}{\omega_n^2 - (r\omega_0)^2} \left(\frac{r\omega_0}{\omega_n} \right) \left[(-1)^r \sin[\omega_n(t - t_e)] - \sin(\omega_n t) \right] \right] \right\} \end{cases} \quad (20)$$

Resonance occurs if $r\omega_0 = \omega_n$, in which case the solution (for $0 \leq t \leq t_e$) is modified according to:

$$\lim_{r\omega_0 \rightarrow \omega_n} \left\{ \frac{\psi_{nr}}{\omega_n^2 - (r\omega_0)^2} \left[\sin(r\omega_0 t) - \frac{r\omega_0}{\omega_n} \sin(\omega_n t) \right] \right\} = \frac{\psi_{nr}}{2\omega_n^2} [\sin(\omega_n t) - (\omega_n t) \cos(\omega_n t)] \quad (21)$$

The proposed technique generalizes the method described in [5], in which eq. (27) represents a particular case of the first of eqs. (17) in the present work. The computational effort of this procedure pertains to the algebraic eigenproblem eq. (6), which has to be solved only once.

2.3. Solution for a non-travelling step force

In the case of a non-travelling step force, the external load density acting on the contact wire in eqs. (1) can be expressed as:

$$f(x, t) = F \delta(x - x_F) u(t - t_0) \quad (22)$$

where u is the unit-step function. The general integral is still given by eqs. (9) and the expression of the particular integral can be found following the previously adopted procedure. Considering a different forcing term \mathbf{f} , in this case constant with respect to time, eq.(10) becomes:

$$\mathbf{M}\ddot{\boldsymbol{\eta}} + \mathbf{K}\boldsymbol{\eta} = \mathbf{f}, \quad \boldsymbol{\eta} = \begin{bmatrix} \boldsymbol{\eta}_1 \\ \boldsymbol{\eta}_2 \end{bmatrix} = \sum_{n=1}^{2N} \mathbf{z}_n p_n(t), \quad \mathbf{f} = F \begin{bmatrix} \boldsymbol{\Phi}(x_F) \\ \mathbf{0} \end{bmatrix} \quad (23)$$

Consequently, eqs. (12) can be rewritten in the form:

$$\ddot{p}_n(t) + \omega_n^2 p_n(t) = \frac{F}{m_n} \sum_{r=1}^N \psi_{nr} \sin\left(\frac{r\pi x_F}{L}\right) \Rightarrow p_n(t) = \frac{F}{m_n \omega_n^2} \sum_{r=1}^N \psi_{nr} \sin\left(\frac{r\pi x_F}{L}\right) \quad (24)$$

The introduction of the initial conditions as in eqs. (15) (zero displacement and zero velocity in $t = t_0$) yields the solution:

$$\begin{cases} w_1(x, t) = F \left\{ \sum_{n=1}^{2N} \alpha_n(x) \alpha_n(x_F) [1 - \cos[\omega_n(t - t_0)]] \right\} u(t - t_0), & \alpha_n(x) = \frac{1}{\omega_n} \sum_{r=1}^N \hat{\psi}_{nr} \sin\left(\frac{r\pi x}{L}\right) \\ w_2(x, t) = F \left\{ \sum_{n=1}^{2N} \beta_n(x) \alpha_n(x_F) [1 - \cos[\omega_n(t - t_0)]] \right\} u(t - t_0), & \beta_n(x) = \frac{1}{\omega_n} \sum_{r=1}^N \hat{\zeta}_{nr} \sin\left(\frac{r\pi x}{L}\right) \end{cases} \quad (25)$$

which represent the time response at a coordinate x due to a force-step of amplitude F applied at a coordinate x_F since $t = t_0$.

2.4. Solution for a non-travelling harmonic force.

In the case of harmonic excitation, the external force density acting on the contact wire in eqs. (1) can be expressed as:

$$f(x, t) = F \delta(x - x_F) \sin[\Omega(t - t_0)] u(t - t_0) \quad (26)$$

where Ω is the angular frequency of the harmonic load. The expression of the particular integral is sufficient to determine the frequency response function. The procedure begins as in eqs. (10) and (23):

$$\mathbf{M}\ddot{\boldsymbol{\eta}} + \mathbf{K}\boldsymbol{\eta} = \mathbf{f}, \quad \boldsymbol{\eta} = \begin{bmatrix} \boldsymbol{\eta}_1 \\ \boldsymbol{\eta}_2 \end{bmatrix} = \sum_{n=1}^{2N} \mathbf{z}_n p_n(t), \quad \mathbf{f} = F \begin{bmatrix} \boldsymbol{\Phi}(x_F) \\ \mathbf{0} \end{bmatrix} \sin[\Omega(t-t_0)] \quad (27)$$

Then, decoupling the equations yields:

$$p_n(t) = G_n \sin[\Omega(t-t_0)] \Rightarrow G_n = \frac{F}{m_n(\omega_n^2 - \Omega^2)} \sum_{r=1}^N \psi_{nr} \sin\left(\frac{r\pi x_F}{L}\right) \quad (28)$$

giving the solution in the form:

$$\begin{cases} G_1(x) = \sum_{n=1}^{2N} \boldsymbol{\Phi}^T \boldsymbol{\Psi}_n G_n \Rightarrow \frac{G_1(x)}{F} = \sum_{n=1}^{2N} \frac{\alpha_n(x) \alpha_n(x_F)}{1 - (\Omega/\omega_n)^2} \\ G_2(x) = \sum_{n=1}^{2N} \boldsymbol{\Phi}^T \boldsymbol{\zeta}_n G_n \Rightarrow \frac{G_2(x)}{F} = \sum_{n=1}^{2N} \frac{\beta_n(x) \alpha_n(x_F)}{1 - (\Omega/\omega_n)^2} \end{cases} \quad (29)$$

which represents a frequency response function (namely, the receptance) at a coordinate x due to a harmonic load of amplitude F and angular frequency Ω acting at a coordinate x_F . As a consequence, the particular integral becomes:

$$\begin{cases} w_1(x, t) = G_1(x) \sin[\Omega(t-t_0)] \\ w_2(x, t) = G_2(x) \sin[\Omega(t-t_0)] \end{cases} \quad (30)$$

The general integral is again the same, given by eqs. (9). The introduction of the initial conditions as in eq. (15) (zero displacement and zero velocity at $t = t_0$) yields the constants A_n and B_n :

$$\begin{aligned} A_n &= F \frac{\boldsymbol{\Phi}^T(x_F) \boldsymbol{\Psi}_n}{m_n} \frac{\Omega}{\omega_n(\omega_n^2 - \Omega^2)} \sin(\omega_n t_0) \\ B_n &= -F \frac{\boldsymbol{\Phi}^T(x_F) \boldsymbol{\Psi}_n}{m_n} \frac{\Omega}{\omega_n(\omega_n^2 - \Omega^2)} \cos(\omega_n t_0) \end{aligned} \quad (31)$$

and then the solution in the form:

$$\begin{cases} w_1(x, t) = F \sum_{n=1}^{2N} \frac{1}{m_n} \left\{ \left[\sum_{r=1}^N \psi_{nr} \sin\left(\frac{r\pi x}{L}\right) \right] \left[\sum_{r=1}^N \psi_{nr} \sin\left(\frac{r\pi x_F}{L}\right) \right] \frac{1}{\omega_n^2 - \Omega^2} \left(\sin[\Omega(t-t_0)] - \frac{\Omega}{\omega_n} \sin[\omega_n(t-t_0)] \right) \right\} \\ w_2(x, t) = F \sum_{n=1}^{2N} \frac{1}{m_n} \left\{ \left[\sum_{r=1}^N \zeta_{nr} \sin\left(\frac{r\pi x}{L}\right) \right] \left[\sum_{r=1}^N \psi_{nr} \sin\left(\frac{r\pi x_F}{L}\right) \right] \frac{1}{\omega_n^2 - \Omega^2} \left(\sin[\Omega(t-t_0)] - \frac{\Omega}{\omega_n} \sin[\omega_n(t-t_0)] \right) \right\} \end{cases} \quad (32)$$

representing the response at a coordinate x to an harmonic excitation of amplitude F and angular frequency Ω acting at a coordinate x_F since $t = t_0$.

3. Finite element method modelling

The proposed method is compared with a FEM of the system in order to evaluate its performance and results. Mass and stiffness matrices are built by considering prismatic homogeneous isotropic Euler–Bernoulli beam elements under axial load, each bringing two nodes and six degrees of freedom [18]. Such an analysis can also provide information on the choice of a numerical integration scheme that matches the dynamic behaviour of the system, which is basically a wave propagation problem. Direct time–integration methods, with known initial conditions, typically fulfil the requests of accuracy and stability, their parameters being the only user defined quantities. The wave propagation nature of the problem makes it difficult to obtain accurate solutions because of spurious accelerations, numerical dispersion and dissipation [19]. Ideally, a time integration method should preserve the real wave velocity, yielding a solution with actual wave modes only. Unfortunately, numerical errors are always present and a method capable of giving small wave speed errors and discarding numerical high frequency modes is desirable. This can be achieved either by introducing numerical damping, which suppresses the high frequency spurious wave modes using an adjustable parameter, or by some inherent properties of integration schemes. Some methods particularly suited to this purposes are available in the technical literature and in the following the Generalized– α method [12] and the Bathe method [11] are considered. Their results are compared with the solutions of the proposed method. The adopted nomenclature is reported in Appendix A.

3.1. Generalized– α method

Proposed by J. Chung and G. M. Hulbert [12], the Generalized– α method uses two parameters, i.e. α_m and α_f , that average the internal and external forces between consecutive time instants, as well as inertia forces. The basic form of the method is given by:

$$\begin{aligned}\mathbf{v}_{n+1} &= \mathbf{v}_n + h\dot{\mathbf{v}}_n + h^2 \left[\left(\frac{1}{2} - \beta \right) \ddot{\mathbf{v}}_n + \beta \ddot{\mathbf{v}}_{n+1} \right] \\ \dot{\mathbf{v}}_{n+1} &= \dot{\mathbf{v}}_n + h \left[(1 - \gamma) \ddot{\mathbf{v}}_n + \gamma \ddot{\mathbf{v}}_{n+1} \right]\end{aligned}\tag{33}$$

$$\hat{\mathbf{M}} \left[(1 - \alpha_m) \ddot{\mathbf{v}}_{n+1} + \alpha_m \ddot{\mathbf{v}}_n \right] + \hat{\mathbf{C}} \left[(1 - \alpha_f) \dot{\mathbf{v}}_{n+1} + \alpha_f \dot{\mathbf{v}}_n \right] + \hat{\mathbf{K}} \left[(1 - \alpha_f) \mathbf{v}_{n+1} + \alpha_f \mathbf{v}_n \right] = (1 - \alpha_f) \hat{\mathbf{f}}_{n+1} + \alpha_f \hat{\mathbf{f}}_n$$

If $\alpha_m = \alpha_f = 0$ the method reduces to Newmark's scheme, whose well known parameters are β and γ . In the general case the resulting time integration algorithm gets second-order accuracy and it is unconditionally stable by setting:

$$\gamma = \frac{1}{2} + \alpha_f - \alpha_m, \quad \beta = \frac{1}{4} (1 + \alpha_f - \alpha_m)^2\tag{34}$$

Furthermore, the two averaging parameters are responsible for numerical damping, which can be controlled introducing the spectral radius at infinity ρ_∞ , related to the amplification matrix of the method [20]. By choosing an appropriate asymptotic spectral radius, the α parameters are simply obtained by:

$$\alpha_m = \frac{2\rho_\infty - 1}{\rho_\infty + 1}, \quad \alpha_f = \frac{\rho_\infty}{\rho_\infty + 1}, \quad \text{with } 0 \leq \rho_\infty \leq 1\tag{35}$$

In the case of null numerical damping ($\rho_\infty = 1$), the method acts like the trapezoidal rule, including high order modes in the solution, while in the case of maximum numerical damping ($\rho_\infty = 0$) a condition known as “asymptotic annihilation” is obtained and spurious oscillations in the high frequencies are eliminated after one time-step. For any other value of ρ_∞ between 0 and 1 the introduced numerical dissipation will filter out a certain range of high frequencies, while preserving accuracy in the low-frequency band.

3.2. Bathe method

Recently K.J. Bathe and G. Noh developed a time integration scheme that, unlike the Generalized- α method, does not require the setting of any parameter, thus the choice of an appropriate step size is enough to damp out numerical high modes [11]. The method divides each time-step into two sub-steps, one solved by means of the trapezoidal rule and the other one solved using

the 3-point Euler backward method, respectively. The equation of motion at time instant t_{n+1} is then split in two sub-equations that can be written in the form:

$$\begin{aligned}\hat{\mathbf{K}}_1 \mathbf{v}_{n+1/2} &= \hat{\mathbf{f}}_1 \\ \hat{\mathbf{K}}_2 \mathbf{v}_{n+1} &= \hat{\mathbf{f}}_2\end{aligned}\tag{36}$$

where:

$$\begin{aligned}\hat{\mathbf{K}}_1 &= \frac{16}{h^2} \hat{\mathbf{M}} + \frac{4}{h} \hat{\mathbf{C}} + \hat{\mathbf{K}} \\ \hat{\mathbf{K}}_2 &= \frac{9}{h^2} \hat{\mathbf{M}} + \frac{3}{h} \hat{\mathbf{C}} + \hat{\mathbf{K}} \\ \hat{\mathbf{f}}_1 &= \hat{\mathbf{f}}_{n+1/2} + \hat{\mathbf{M}} \left(\frac{16}{h^2} \mathbf{v}_n + \frac{8}{h} \dot{\mathbf{v}}_n + \ddot{\mathbf{v}}_n \right) + \hat{\mathbf{C}} \left(\frac{4}{h} \mathbf{v}_n + \dot{\mathbf{v}}_n \right) \\ \hat{\mathbf{f}}_2 &= \hat{\mathbf{f}}_{n+1} + \hat{\mathbf{M}} \left(\frac{12}{h^2} \mathbf{v}_{n+1/2} - \frac{3}{h^2} \mathbf{v}_n + \frac{4}{h} \dot{\mathbf{v}}_{n+1/2} - \frac{1}{h} \dot{\mathbf{v}}_n \right) + \hat{\mathbf{C}} \left(\frac{4}{h} \mathbf{v}_{n+1/2} - \frac{1}{h} \mathbf{v}_n \right)\end{aligned}\tag{37}$$

Accelerations, velocities and displacements are computed using the typical equations of trapezoidal and Euler backward methods. The resulting algorithm is an implicit second-order accurate scheme, capable of discarding numerical modes provided that the time step is appropriately selected.

To achieve some insight on the choice of the time step, the simple case of travelling wave (given by the d'Alembert equation in one dimension) is considered. If c_0 is the wave velocity, the resulting Courant–Friedrichs–Lewy number (CFL) will be:

$$\text{CFL} = c_0 \frac{h}{l}\tag{38}$$

CFL relates the ratio between element size l and time-step h (i.e. a velocity) to the speed of the travelling information in the physical space. If an explicit time integration solver is used, then the choice of this value is crucial in order to guarantee stability in the solution, and the condition is usually $\text{CFL} \leq 1$. On the contrary, implicit time integration algorithms are usually less sensitive to numerical instability and larger values of CFL may be tolerated. It is important to highlight that in general the stability of the response does not ensure its physical correctness [20].

For the Bathe method a relation between the values of the CFL number, the wavenumber k (related to the frequency ω of the wave mode) and the element size l can be obtained. In particular,

setting $CFL = 1$ will produce all wave modes having $h\omega \cong kl < 0.6\pi$ to be almost non-dispersive (meaning that the wave speed has not significant alterations), whereas all higher frequency modes will be dissipated [19].

4. Numerical examples: Application to overhead contact lines

The proposed method can easily be adapted to railway overhead contact lines, simply by considering the characteristics of the messenger wire, contact wire, steady arms and droppers. In the following section the data reported in the standards EN50318 [13] and EN50149 [21] will be adopted.

4.1. Non-travelling step force in a contact wire

Recalling an example presented in [9], a step excitation of magnitude f is applied to a pinned-pinned contact wire. The force acts at a distance x_F from one support, and the acceleration is measured at a distance x_M , as shown in Fig. 2.

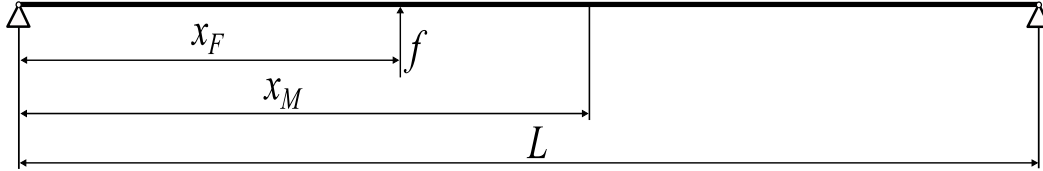


Fig. 2. Definition of the test problem: non-travelling step force in a contact wire, where $L = 200$ m, $x_F = 95$ m, $x_M = 135$ m, $\mu = 1.35$ kg/m, $EI = 168$ Nm², $T = 20$ kN, $f = 100$ N.

An analytical undamped solution to this problem has been already found in [7, 9], and it can be derived from eq. (25) of the presented method if only one beam is considered.

The first $N = 400$ terms are considered in the proposed method: this modal truncation is the only source of error in this case, since the comparison functions adopted in eq. (3) are, in fact, the eigenfunctions for this system.

In this case, the equation of the wave speed can be rewritten as a function of the considered modes [5]:

$$c_j = \sqrt{\left(\frac{j\pi}{L}\right)^2 \frac{EI}{\mu} + \frac{T}{\mu}} \quad j=1,2,3,\dots \quad (39)$$

As a direct consequence, the definition given for CFL in eq. (38) cannot be used as a unique reference. The wave speed of the 400th mode can rather be taken as an upper limit for the modes included in the solution, and the damping properties of the numerical algorithms can be analysed separately. The CFL related to this choice is then called CFL_N.

As discussed previously, the purpose of the presented paper is to analyse the effects of the numerical damping introduced by the integration algorithms, and to rely on it to handle numerical spurious modes. Indeed, structural damping has also the effect of bounding numerical modes, but this should be considered as a property of the system, rather than a parameter to be tuned. Moreover, railway overhead contact lines are low-damped systems, and the introduction of structural damping in absence of numerical damping is not sufficient to suppress spurious modes. A further investigation about this point may be conducted considering the system depicted in Fig. 2 and adding a realistic amount of proportional damping. This kind of damping is generally described by means of two parameters α and β , that allow the damping ratio ζ_j of the j^{th} mode to be written as:

$$\zeta_j = \frac{\alpha}{2\omega_j} + \frac{\beta\omega_j}{2} \quad (40)$$

Where ω_j is the j^{th} undamped natural frequency, $\alpha = 0.06$, $\beta = 6 \cdot 10^{-6}$ [22]. Fig. 3 shows a comparison between the presented method and the Generalized- α method with and without structural damping respectively. The adopted discretization is summarized in Table 2, without numerical damping in both cases. Numerical modes arise especially in the undamped case, and structural damping can only weaken their effects. It seems then appropriate not to rely on it to remove numerical modes; thus, for the purpose of this investigation, only numerical damping is considered in the following sections.

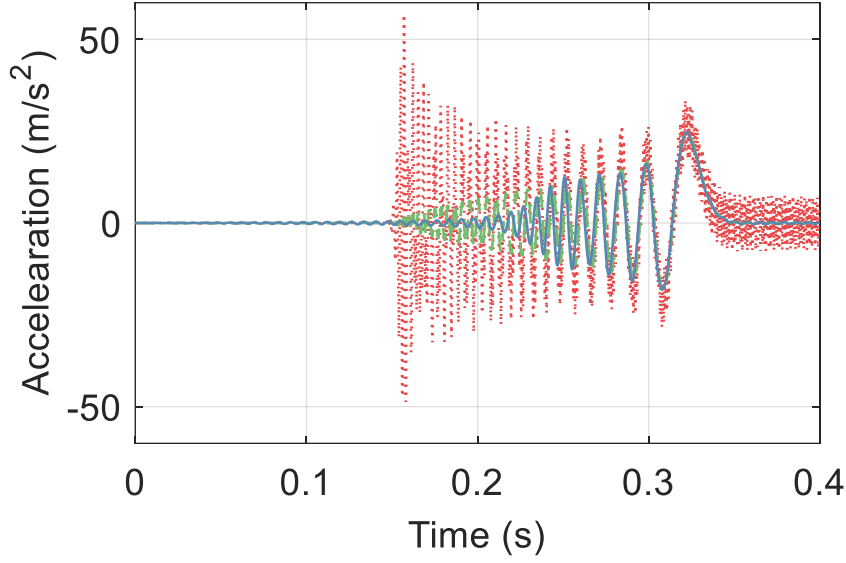


Fig. 3. Acceleration of the measuring point x_M . Solid blue line: proposed method with proportional damping; dashed red line: Generalized- α method with no numerical damping and no structural damping; dashed-dotted green line: Generalized- α method with no numerical damping and with proportional (structural) damping.

As already shown, the Bathe method is capable of discarding high spurious modes in relation to the discretization used: fixing the value of l and lowering h will cause the method to include an increasing number of participating wave modes, meaning that a compromise between desired accuracy and numerical damping should be found. Taking the analytical method as a reference, a parametric study is summarized in Table 1, where l and h are chosen so to obtain $CFL_N=1$ in each case. Two indices are used to evaluate the performance, the wave distortion and the root mean square (RMS) error between the acceleration computed with the presented method and the Bathe method. The wave distortion is computed evaluating the maximum cross correlation between the two accelerations (here called \ddot{w}_1 and \ddot{w}_2) according to eq. (41). The final time interval is chosen according to Table 2 and the results are reported in Fig. 4a.

$$R_{\ddot{w}_1 \ddot{w}_2}(\tau) = E[\ddot{w}_1(t)\ddot{w}_2(t+\tau)] \quad (41)$$

Table 1. Period shift and RMS error for the Bathe method in numerical example 4.1.

Element size l (m)	Time step h (ms)	Wave distortion (ms)	RMS error (m/s ²)
0.10	0.7	-2.1	3.6329
0.08	0.5	-1.3	4.1278
0.05	0.3	-0.7	4.6324
0.03	0.2	-0.2	5.6019

The Generalized- α method is based on the trapezoidal rule, therefore the suggestions reported in [11] are followed to set its discretization, considering $CFL_N=0.65$. The final values are reported in Table 2. As mentioned above, its damping properties depend on the value of the asymptotic spectral radius, whose effects can be clearly seen in Fig 3 and Fig. 4: without numerical damping spurious accelerations arise, especially around the wave front. Generally speaking, the introduction of manually controlled numerical dissipation is a powerful solution, however it is not an easy choice when dealing with complex systems, or when a comparative model is not available. These cases should then be tackled by a trial-and-error procedure, which is at least time consuming.

Table 2. Discretization adopted in numerical example 4.1

	Generalized- α method	Bathe method
Element size l (m)	0.08	0.08
Time step h (ms)	0.37	0.5

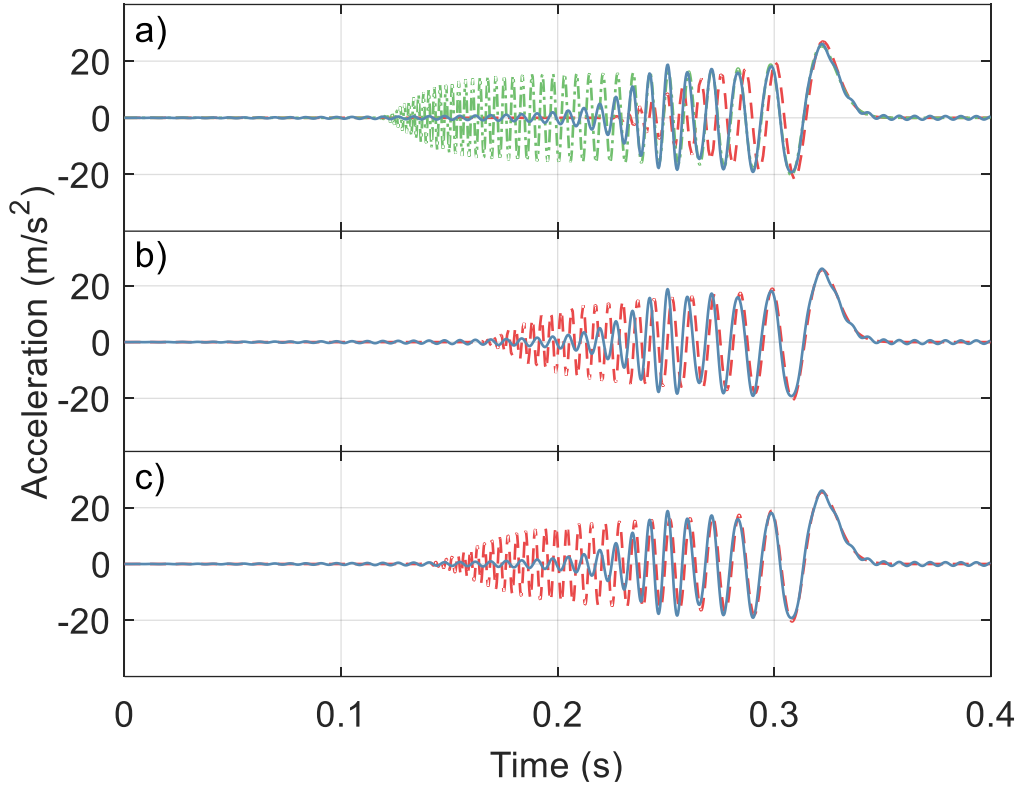


Fig. 4. Acceleration of the measuring point x_M .

- a) Solid blue line: proposed method; dashed red line: Bathe method ($l=0.1$ m, $h=7 \cdot 10^{-4}$ s); dashed-dotted green line: Bathe method ($l=0.03$ m, $h=2 \cdot 10^{-4}$ s);
b) Solid blue line: proposed method; dashed red line: Bathe method ($l=0.08$ m, $h=5 \cdot 10^{-4}$ s);
c) Solid blue line: proposed method; dashed red line: Generalized- α method ($\rho_\infty = 0.4$, $l=0.08$ m, $h=3.7 \cdot 10^{-4}$ s).

4.2. Forced harmonic vibrations in the contact wire

Considering again the system of Fig. 2, a harmonic force $f = F \sin(\Omega t)$ is applied with $F=10$ N and $\nu = \Omega/(2\pi)=50$ Hz. The force acts at a distance x_F from one support, and the acceleration is measured at a distance x_M .

The modal truncation is again $N=400$ in the proposed method, while discretizations are adopted yielding $CFL = 1$ for the Bathe time integration algorithm, and $CFL = 0.65$ for the Generalized- α method (with no numerical damping) [11]. In order to evaluate the CFL, the element size is set according to Table 3 and the wave speed c is computed with the following equation [3]:

$$c = \sqrt{\frac{T + \sqrt{T^2 + 4\mu EI \Omega^2}}{2\mu}} \quad (42)$$

The wavelength related to the forcing oscillation is then equal to 2.5 m, while the wavelength of the 400th mode, whose velocity can be computed by eq. (39), is 1 m. As the load starts acting at time $t = 0$ s, two waves travel from x_F pointing to the right and to the left, hereinafter called “*RTW*” (Right Travelling Wave) and “*LTW*” (Left Travelling Wave). After 0.3202 s the *RTW* meets the measuring point, while the *LTW* reaches the left end point and comes back, interfering with the wave produced by the load. It is very interesting to notice what happens when *LTW* reflects, because if numerical errors are present when computing the acceleration due to a single travelling wave, these errors will allegedly sum up when dealing with reflected waves. Table 3 summarizes the parameters used in the integration schemes.

Table 3. Discretization adopted in numerical example 4.2

	Generalized- α method	Bathe method
Element size l (m)	0.05	0.05
CFL	0.65	1
Resulting time step h (s)	$2.6 \cdot 10^{-4}$	$4 \cdot 10^{-4}$

The time history of the acceleration is given in Fig. 5, using eq. (32) of the presented method.

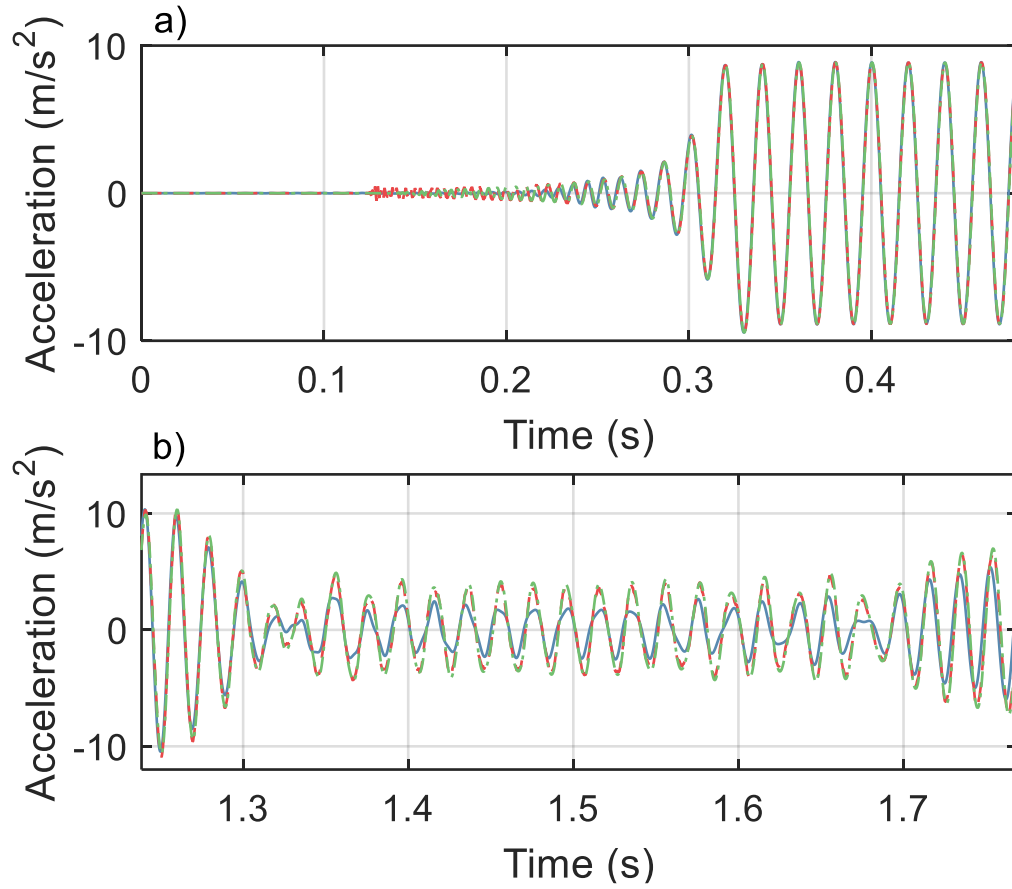


Fig. 5. Acceleration of the measuring point x_M during two time windows: a) before the *RTW* meets the measuring point (0.3202 s), b) after the reflected *LTW* meets the measuring point (1.3610 s). Solid blue line: proposed method; dashed red line: Generalized- α method (no numerical damping); dashed-dotted green line: Bathe method.

During the initial transient the Generalized- α method shows little spurious accelerations because of the absence of numerical damping, while the Bathe method automatically discards numerical high modes. However, after the initial transient they both perform very well if a single travelling wave is present (Fig. 5a).

When the first reflection occurs, the three methods perform quite differently (Fig. 5b). For a deeper analysis, a particular case may be considered: the loading point position x_F is selected as an integer multiple of the wavelength related to the harmonic excitation. This will theoretically cause a destructive interference when the *LTW* meets the measuring point, giving null acceleration till the second reflection occurs. Furthermore, x_F and x_M are two nodes in the FE model.

The selected values are the wavelength $\lambda = c/n = 1.89$ m and the distance $x_F = 5\lambda$. The *RTW* will meet the measuring point after 0.3143 s, while the destructive interference will occur at $t = 0.4629$ s. Two time screenshots of the acceleration along the wire, computed with the presented method, are given in Fig. 6. It can be seen that at $t = 0.93$ s the acceleration of the measuring point is almost negligible, as expected.

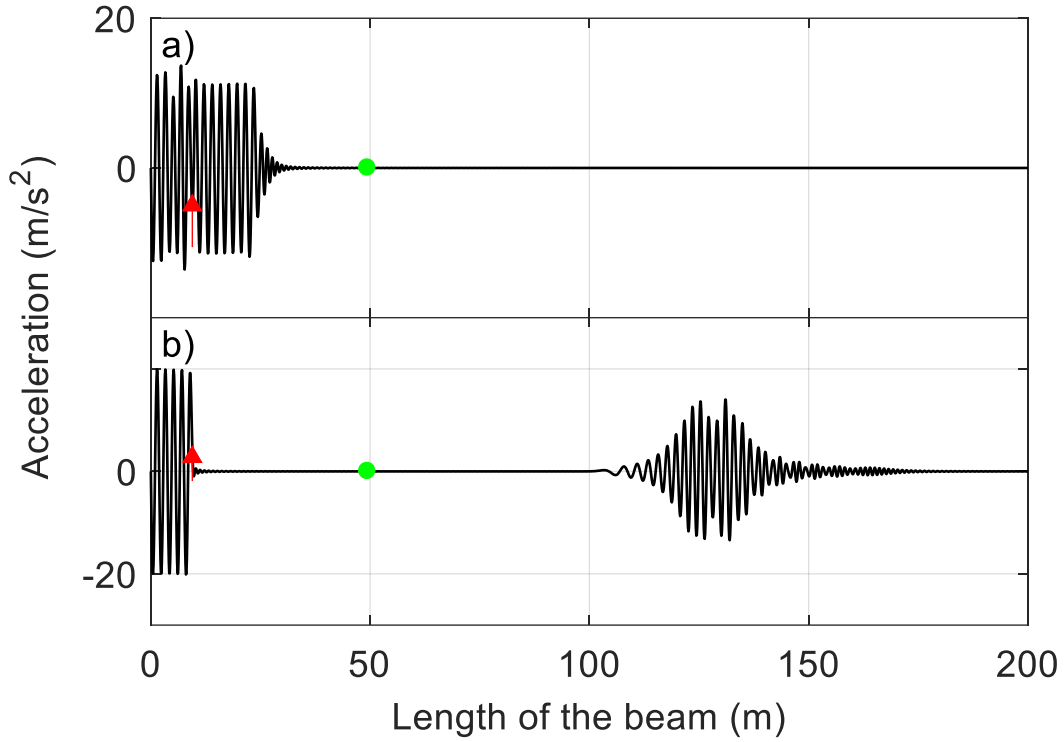


Fig. 6. Two screenshots of the acceleration along the contact wire for the proposed method: a) $t = 0.11$ s, before the *RTW* meets the measuring point; b) $t = 0.92$ s, after the first reflection; red arrow: load point; green dot: measuring point.

Comparing now the acceleration computed with the finite element methods, it can be seen in Fig. 7 that small errors are present, especially for the Generalized- α method with no numerical damping. Furthermore, the numerical wave speed and the numerical wave number can be extracted from the time history, so a comparison is reported in Table 4.

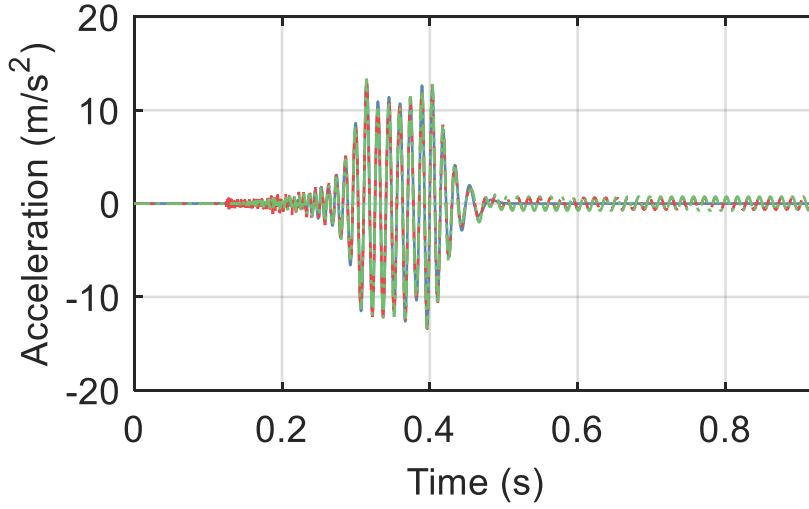


Fig. 7. Acceleration of the measuring point x_M . Solid blue line: proposed method; dashed red line: Generalized- α method (no numerical damping); dashed-dotted green line: Bathe method.

Table 4. Comparison between theoretical and numerical wave speed and wave number.

	Analytical	Proposed method	Generalized- α	Bathe
Wave speed (m/s)	127.2482	127.2482	127.3278	127.2482
Error (%)	-	0	0.0625	0
Wave number (m^{-1})	0.5291	0.5298	0.5302	0.5298
Error (%)	-	0.1325	0.2026	0.1325

4.3. Moving load in a simplified overhead contact line and considerations on the influence of the bending stiffness

A further step towards the analysis of a complete overhead contact line is made by considering the simplified catenary system shown in Fig. 8, without lumped masses. The load travels at 300 km/h through two spans 60 m long each, with constant modulus $P = 200$ N. The proposed method has been applied with a modal truncation at approximately 300 Hz ($N = 400$), while the discretization adopted in the two FE models is obtained following the same procedure used so far. CFL_N is set to 1 for the Bathe method, and to 0.65 for the Generalized- α method. In this case the wave speeds of the upper and lower wires are slightly different, so the minimum resulting h has been selected, following eq. (38). The final values are reported in Table 5.

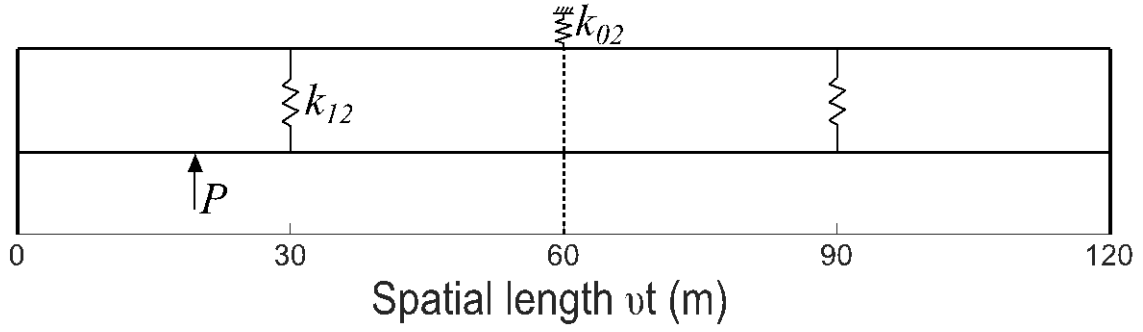


Fig. 8: Definition of the test problem: moving load in a simplified overhead contact line, where $P = 200$ N, $k_{12} = 10^5$ N/m, $k_{02} = 10^{10}$ N/m, $v = 300$ km/h, $\mu_1 = 1.35$ kg/m, $\mu_2 = 1.07$ kg/m, $EI = 168$ Nm², $T_1 = 20$ kN, $T_2 = 16$ kN.

Table 5. Discretization adopted in numerical example 4.3

	Generalized- α method	Bathe method
Element size l (m)	0.08	0.08
Time step h (ms)	0.30	0.47

In this case, because of the presence of elastic elements k_{12} and k_{02} , the solution computed with the presented method is an approximation of the solution to the equilibrium eqs. (1), obtained using the comparison functions in eqs. (3). Before starting the time domain analysis, it is thus useful to investigate the frequency domain, comparing the natural frequencies and mode shapes of the structure, computed with both the proposed method and the finite element model. Since only transverse modes are taken into account in this study, the eigenvalues and eigenvectors related to the other degrees of freedom computed with the FE model are discarded. The natural frequencies of the contact wire are shown in Fig. 9, while the Modal Assurance Criterion of the first 6 modes is represented in Fig. 10.

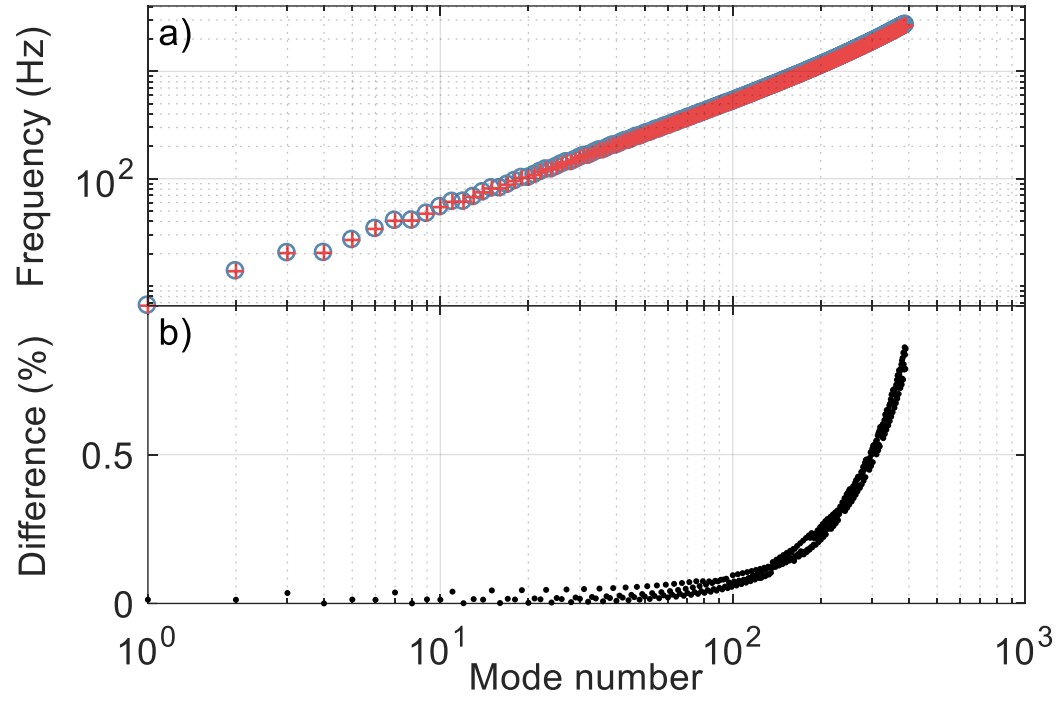


Fig. 9: Natural frequencies of the contact wire. a) Blue circles: proposed method; red crosses: FE method. b) Difference (%) between the two methods.

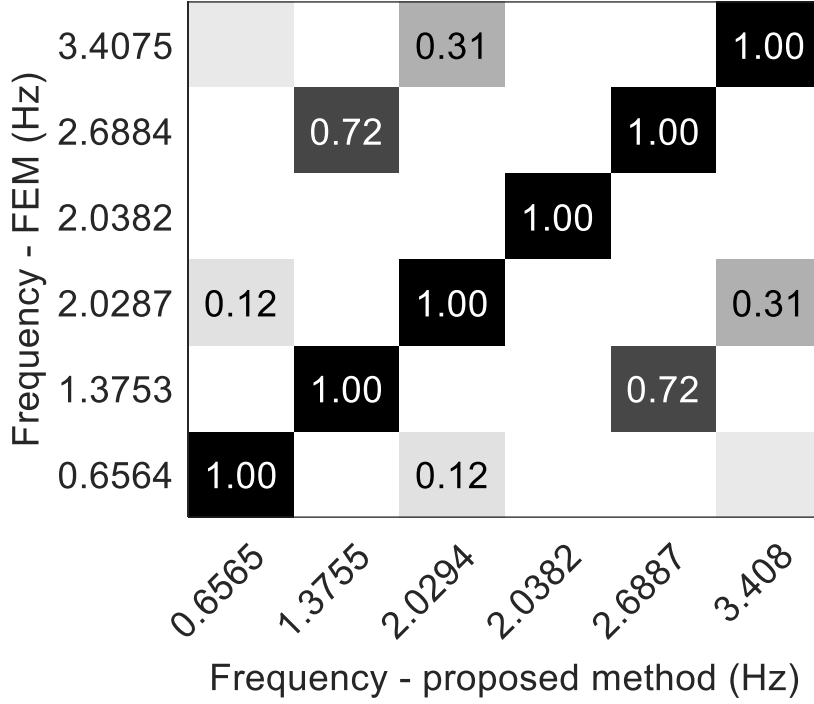


Fig. 10: Modal Assurance Criterion of the first 6 modes.

Because of the high degree of consistency in both frequencies and mode shapes, time histories can be compared. Only the displacement and the acceleration given by the presented method are shown, since the displacements computed with the three different methods overlap almost perfectly, and the previous considerations on the accelerations still hold. In particular, Fig. 11 shows the evolution of the system at different time instants, while Fig. 12 shows the displacement and the acceleration of the contact wire at a distance $x_M = 20$ m. Also, the total stress exerted on the contact wire is represented. This is essentially composed by two components: the normal stress, i.e. the ratio of the tensile force to the area of the section, and the dynamic oscillations related to the bending of the wire. The latter is obtained evaluating the bending moment:

$$M_1 = -K_1 \frac{\partial^2 w_1(x, t)}{\partial x^2} \quad (43)$$

where $\partial^2 w_1(x, t) / \partial x^2$ is the curvature of the contact wire, which can be analytically derived from eqs. (17) and (20).

The total stress is then:

$$\sigma = \frac{T}{A} + \frac{M(x,t)z}{I}, \quad 0 \leq z \leq \frac{d}{2} \quad (44)$$

where z is the vertical coordinate along the transverse section of the wire and has its maximum on the upper and lower borders.

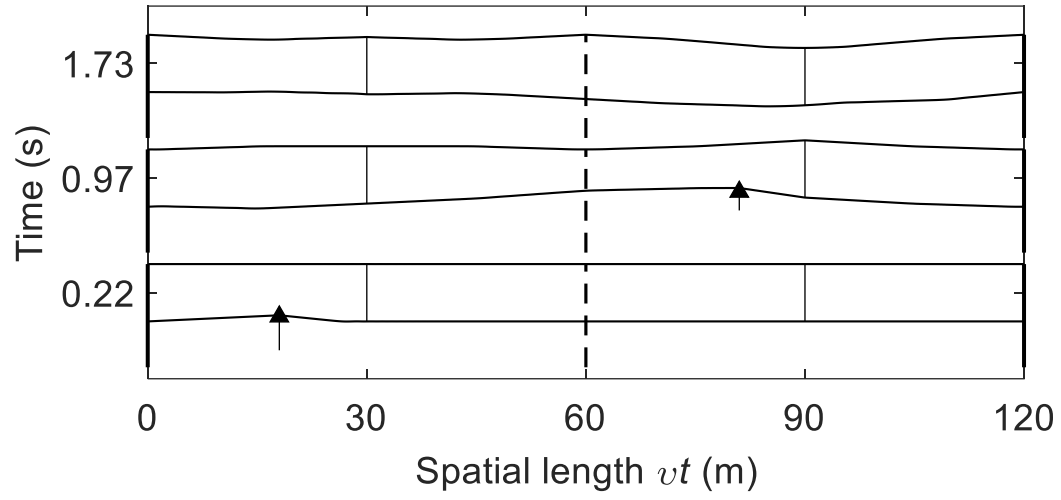


Fig. 11: Time evolution of the simplified overhead contact line model. Vertical arrows indicate the position of the load P.

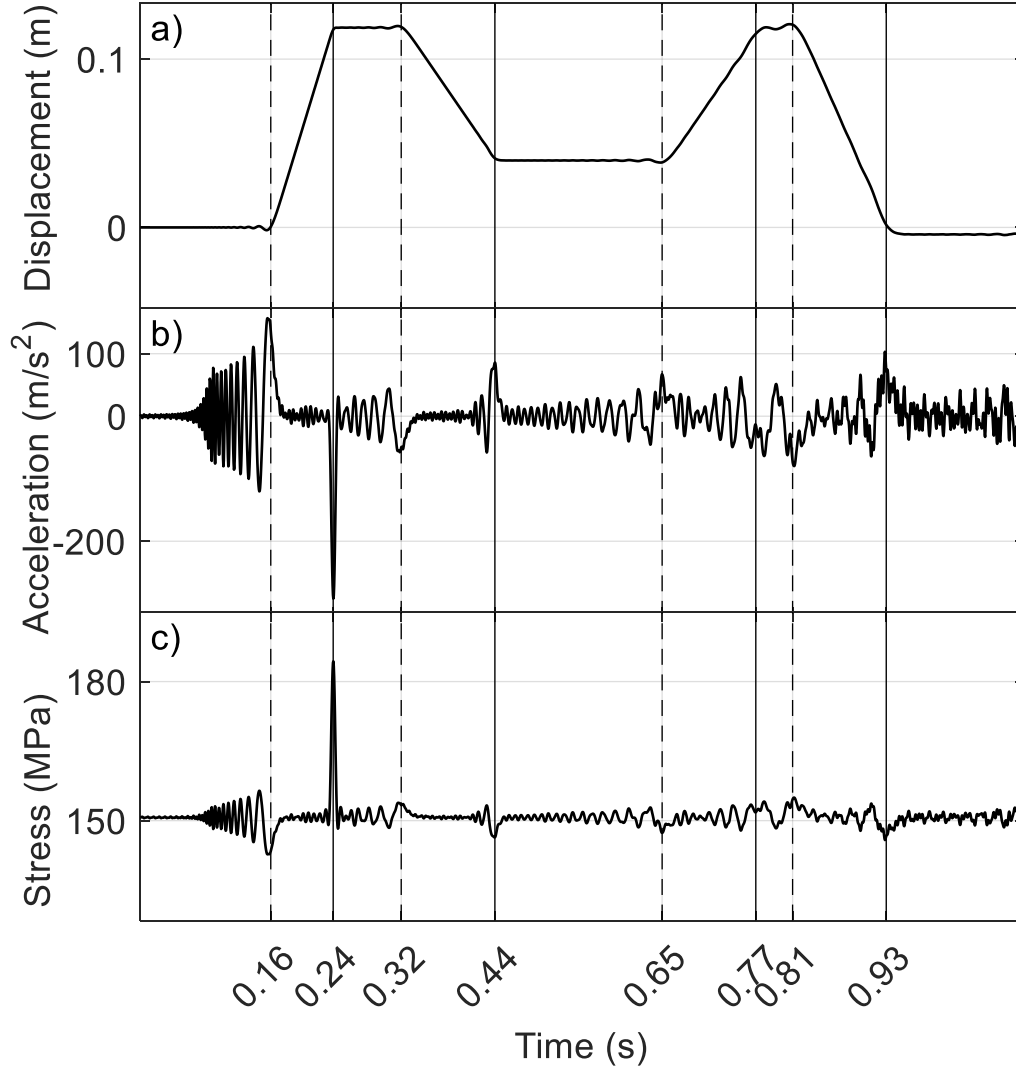


Fig. 12: Results of the presented method for the measuring point $x_M = 20$ m. a) Displacement of the contact wire. b) Acceleration of the contact wire. c) Stress of the contact wire. Dashed vertical lines: time instants when the lowest speed wave meets the measuring point. Continuous vertical lines: time instants when either the load or the waves reflected due to the load meet the measuring point.

A considerable part of the stress is due to the axial load and is constant, while the stress related to bending is variable. The dynamic stress is not negligible and provides a 20% increment of the total stress when the pantograph meets the measuring point. When a string model is adopted for the two wires (instead of a Euler-Bernoulli beam model), their bending stiffness becomes null and the resulting total stress is associated only to the axial force. The string model can be obtained in the presented method by setting $K = 0$ for both the contact wire and the messenger

wire and leads to a non-dispersive wave propagation, i.e. to a constant wave speed. The effect can be seen in Fig. 13, showing a comparison between the two approaches in terms of acceleration. This is the simplest wave propagation model and it is acceptable in many engineering problems. In the specific case of railway contact lines, the axial force is dominant and the bending stiffness can be neglected for low velocities of the pantograph. At high speeds, however, the bending stress might be important [5], as the fatigue fracture is one of the most critical failures in this framework [23]. The most stressed areas of the overhead contact line can be recognized in Fig. 14, which shows two contour plots of the total stress for the contact wire and the messenger wire. It appears that the bending stress is particularly relevant in the areas close to the support of the messenger wire (60 m), close to the droppers (30 m and 90 m), and in contact with the pantograph.

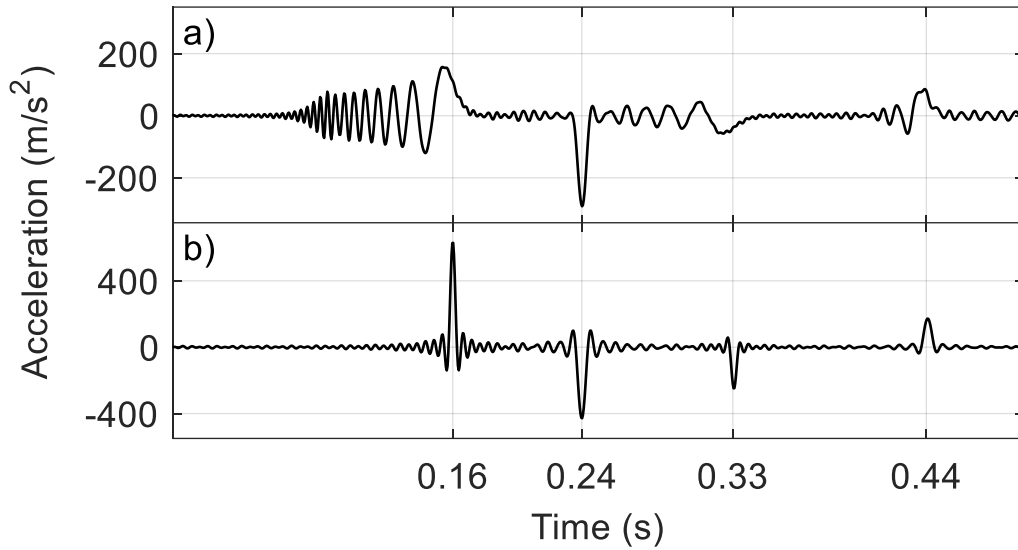


Fig. 13: Acceleration of the contact wire for the measuring point $x_M = 20$ m. a) Non-zero bending stiffness $K = EI$; b) Zero bending stiffness $K = 0$.

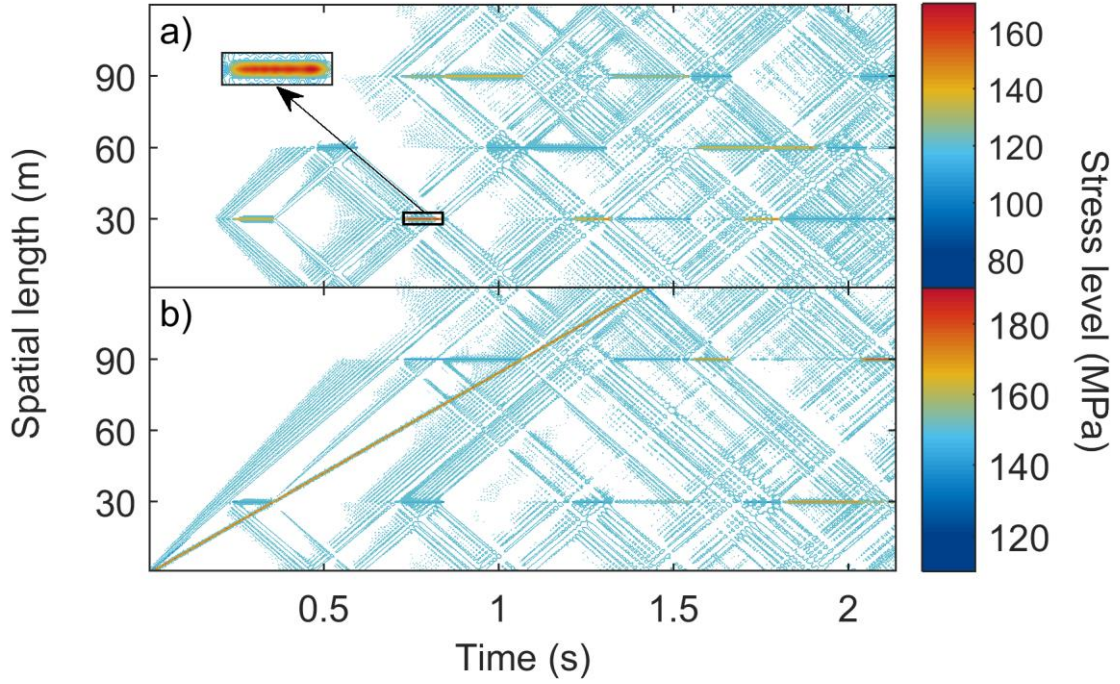


Fig. 14: Contour plot of the total stress in the spatial-time domain. a) Stress on the messenger wire. b) Stress on the contact wire.

Fig. 14 gives also a representation of the propagation and the reflections of the waves that occur along the two wires, whose deeper analysis is suggested as follows. Referring to Fig. 12, as the load starts to travel at time $t_0 = 0$ s with velocity v , waves propagate from the zero position. The slowest wave with speed c_1 will meet the measuring point after a time $t_{1c} = x_M / c_1 \cong 0.16$ s, when a change of slope in the displacement can be clearly observed. Before this instant, the acceleration oscillates with an increasing period, meaning that higher wave modes travel faster, as expected. The moving load will meet the measuring point after a time $t_{1v} = x_M / v \cong 0.24$ s, when another change of slope in the displacement can be observed, and when the acceleration shows a great discontinuity. After t_{1u} reflections will occur due to both the propagation of the initial waves and the waves that start travelling each time the moving load meets an elastic connection (i.e. a dropper). In order to highlight the first reflections, a scheme is provided in Fig. 15.

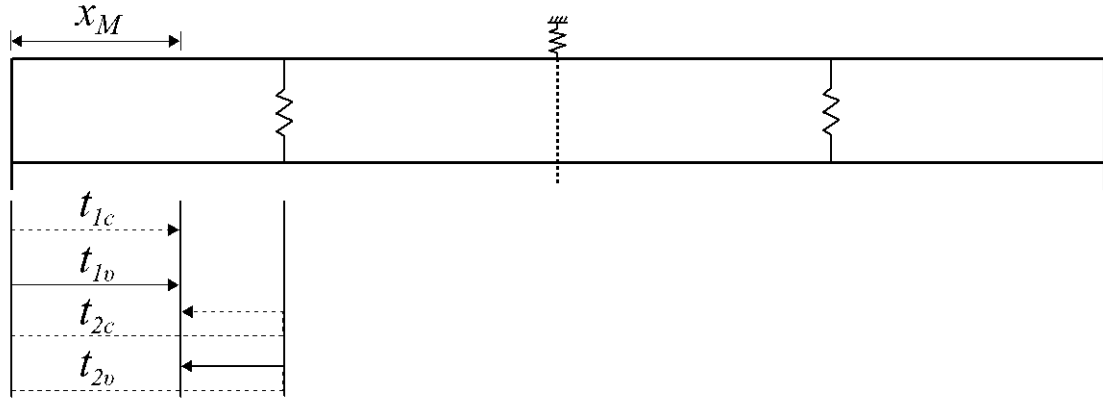


Fig. 15: Wave reflections related to the measuring point. Dashed arrows: time instants when the lowest speed wave meets the measuring point. Continue arrows: time instants when either the load or the waves reflected due to the load meet the measuring point.

At each indicated instant (t_{1c} , ..., t_{2v}), as well as in following ones, a change of slope occurs in the displacement. This phenomenon is quite easily observed if just a small number of waves is considered. But it becomes more difficult to interpret when more waves start interfering, as it can be clearly observed in the acceleration time history of Fig. 12b.

4.4. Dynamics of a complete overhead contact line under a moving load

Finally, the dynamics of a complete catenary is investigated: ten spans are taken into account, 60 m long each and including nine non-equally spaced droppers, according to [13]. Furthermore, there are two lumped masses on each dropper, representing the inertia of the dropper with its clamps, and a lumped mass at the end of each span in the contact wire, representing the inertia of the registration arm. The system is shown in Fig. 16; the representation of the lumped masses is omitted. A similar system is studied in the benchmark proposed in [24] with the aim of studying the pantograph-catenary interaction.

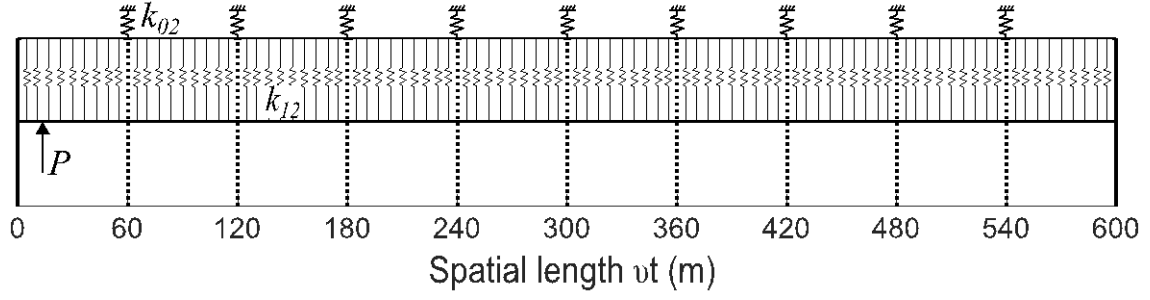


Fig. 16: Definition of the test problem: Dynamics of a complete overhead contact line under a moving load. $P = 200$ N, $k_{l2} = 10^5$ N/m, $k_{o2} = 10^{10}$ N/m, $v = 300$ km/h, $\mu_1 = 1.35$ kg/m, $\mu_2 = 1.07$ kg/m, $EI = 168$ Nm², $T_1 = 20$ kN, $T_2 = 16$ kN, $m_0 = 0.33$ kg, $m_{l2} = 0.2$ kg.

All the phenomena discussed so far still are present, but they are not straightforward to observe due to the complexity of the considered system. In fact, reflections will occur almost as the load starts moving and the resulting acceleration time history is difficult to interpret, as can be seen in Fig. 17a, which shows the acceleration of the contact wire at 60 m. The proposed method has been applied with a modal truncation at approximately 300 Hz ($N = 2000$), while the discretization of the FE model is the same of the previous case (Table 5). The probability distributions of the shown time histories are provided in Fig. 17b, while the statistical parameters are listed in Table 6. Some samples are distinctly out of a normal distribution for the following two reasons: the zero value before the arrival of the first waves, with a positive excess of kurtosis (3 being the kurtosis of the normal distribution); the peak caused by the load is related to the slightly negative skewness. Furthermore, the second and the third rows of Table 6 show the results obtained when a 10th order Butterworth band-pass filter is applied to the time history computed with the proposed method and the FE model (Bathe), acting in the frequency band 0-20 Hz and 20-300 Hz respectively.

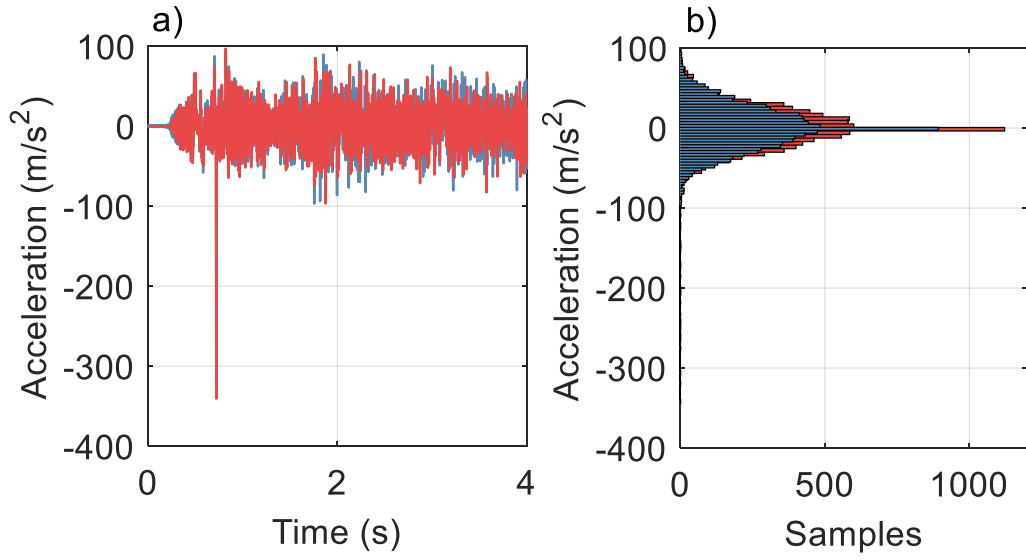


Fig. 17: Acceleration of the contact wire at 60 m. a) Time domain - blue line: proposed method, red line: Bathe method. b) Probability distribution - blue bars: proposed method, red bars: Bathe method.

Table 6: Statistical parameters of the acceleration with the proposed method and the Bathe method.

		Proposed method	Bathe method
Original data	Mean value μ (m/s^2)	0.0629	0.0642
	Standard deviation σ (m/s^2)	28.0166	26.0793
	Maximum value (m/s^2)	94.9488	97.0298
	Minimum value (m/s^2)	-264.6728	-340.6061
	Skewness	-0.6263	-0.9591
	Excess of kurtosis	5.1967	10.8141
Filtered data (0-20 Hz)	Mean value μ (m/s^2)	0.0936	0.1224
	Standard deviation σ (m/s^2)	8.2554	8.2540
	Maximum value (m/s^2)	33.9019	33.9094
	Minimum value (m/s^2)	-35.0706	-35.1372
	Skewness	-0.0716	0.0312
	Excess of kurtosis	1.5149	1.5743
Filtered data (20-300 Hz)	Mean value μ (m/s^2)	-0.01878	0.01926
	Standard deviation σ (m/s^2)	26.9220	22.2560
	Maximum value (m/s^2)	98.1242	81.0812
	Minimum value (m/s^2)	-177.6214	-241.3405
	Skewness	-0.0709	-0.3584
	Excess of kurtosis	0.2253	1.9097

It can be seen that the probability distributions of the two time histories are similar, especially if higher frequencies are filtered out. This statement is in agreement with the previous results, and it is confirmed by Fig. 18a, that shows the power spectral density (PSD) of the acceleration computed by the presented method and its absolute difference with respect to the PSD computed by the Bathe method. As expected, the difference is negligible at low frequencies, in particular up to 20–30 Hz, while it becomes relevant at higher frequencies.

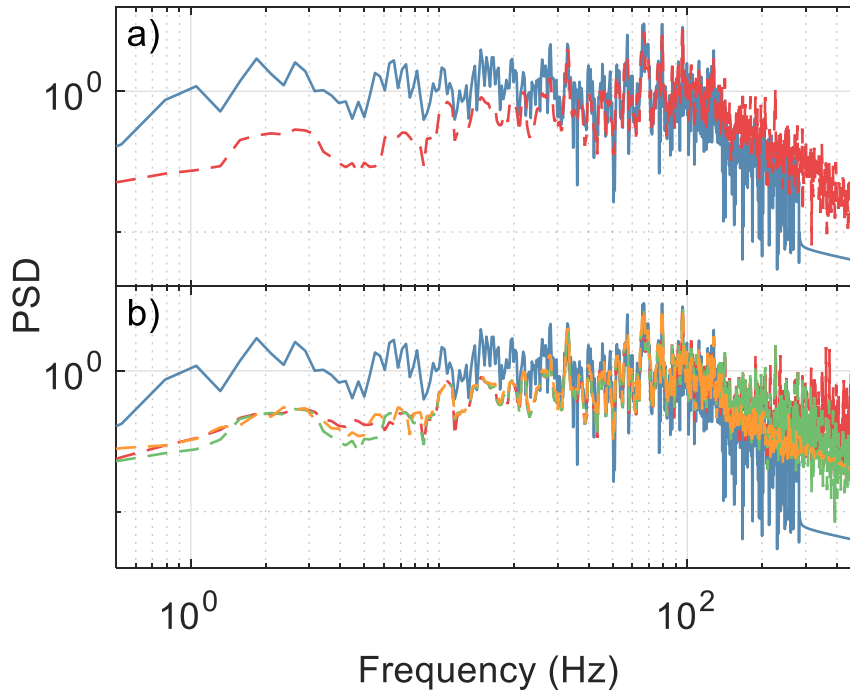


Fig. 18: Power spectral density of the acceleration of the contact wire at 60 m. a) Solid blue line: presented method; dashed red line: difference between the presented method and the Bathe method. b) Solid blue line: presented method; dashed red line: difference between the presented method and the Generalized- α method, with $\rho_\infty=1$; dashed green line: difference between the presented method and the Generalized- α method, with $\rho_\infty=0.7$; dashed yellow line: difference between the presented method and the Generalized- α method, with $\rho_\infty=0.2$.

Discrepancies at high frequencies may depend on the settings of the two methods (modal truncation for the proposed method and temporal/spatial discretization for the Bathe method), as well as possible numerical dispersion and dissipation. However, the current standard EN50318 [13] limits the frequency range of interest to 20 Hz for a 10 spans overhead contact line. The structural configuration is responsible for a high modal density (hundreds of modes in this fre-

quency range) as can be seen in Fig. 19, which shows the punctual receptance of the contact wire computed using eq. (29) when a harmonic load is applied at 60 m.

These considerations are still valid when using the Generalized- α method, and it is appropriate to use the presented method as a comparison in order to select the optimum value of the asymptotic spectral radius ρ_∞ for this specific case. According to numerical simulations, the best results are achieved if $\rho_\infty \approx 0.65$ - 0.75 for a 10 spans railway catenary system. Indeed, an excessive increase in the numerical damping (i.e. $\rho_\infty \rightarrow 0$) would cause a loss of information in the frequency range of interest, while an excessive reduction (i.e. $\rho_\infty \rightarrow 1$) would generate high spurious modes. In both cases the method would produce an erroneous representation of the system dynamics. Fig. 18b shows the power spectral density (PSD) of the acceleration computed by the presented method and its absolute difference with respect to the PSD computed by the Generalized- α method for three different values of the spectral radius ρ_∞ .

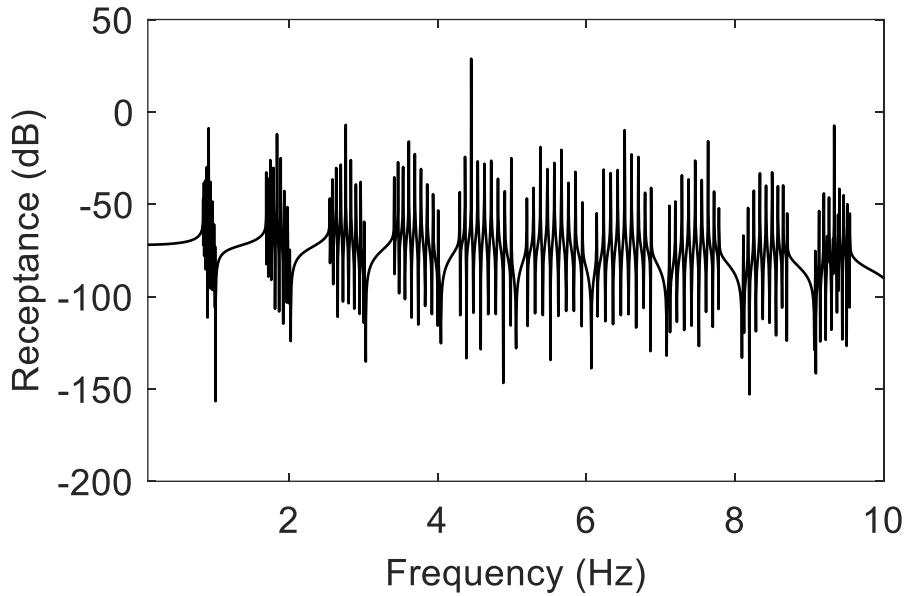


Fig. 19: Punctual receptance of the contact wire when a harmonic load is applied at 60 m.

Finally, the evolution of the system in terms of displacements within different time instants is represented in Fig. 20. Only the results given by the presented method are shown: the displacements computed using the three considered methods are almost equal if proper integration parameters are selected. The numerical cost for the two approaches is different from a computa-

tional point of view. Indeed, time integration schemes may require a low time step and a fine spatial discretization to obtain the desired accuracy. By contrast, the presented method is not based on a computation over time so the time step can be increased without affecting the accuracy of the solution. Also, the solution can be computed only in the points of interest, and the calculation can be very easily parallelized, each response being independent from the previous. In this context, the simulation runs in 4-6 minutes for the three methods on the same CPU.

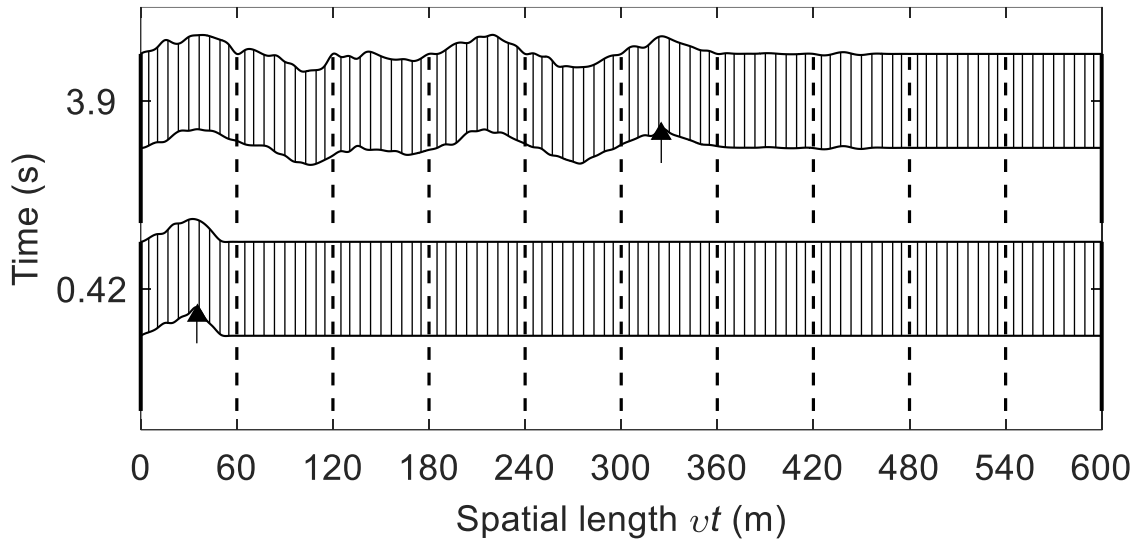


Fig. 20: Time evolution of the complete overhead contact line model.

5. Conclusions

A distributed parameter model for wave propagation in two-level catenary systems has been developed and validated by means of numerical examples. The wires are modelled as two straight axis parallel beams forced by the moving load applied by the pantograph. The general solution is sought by an application of the Ritz–Galerkin method, leading to a form that automatically discards higher frequency modes. Although the proposed method can be extended to several configurations, the aim of this paper was to provide a valid reference for time integrations of finite element models of railway overhead contact lines. Two different integration schemes have been considered: the Generalized- α method and the Bathe method. As a general rule, the solution sought by a FEM is always affected by numerical errors due to the discretization adopted. In the present study it has been highlighted how in the considered system numerical errors are mostly related to spurious wave modes. The behaviour of both methods has been investigated in different cases, taking the presented model as a reference. It is observed that as waves travel, the errors related to wave velocities and amplitudes can accumulate, thus producing a very erroneous numerical solution.

Results have shown that errors produced by the FE models can be reduced implementing a numerical dissipation technique, provided that a proper adjustment to the case study is performed. Some considerations about the settings of the integrations schemes have therefore been discussed, eventually obtaining a set of optimum parameters for the two algorithms. Particular attention has been paid to the coupled dynamics of a complete overhead contact line. Indeed, optimal settings for this kind of systems are crucial in the investigation of pantograph-catenary contact dynamics, especially when considering a pantograph travelling at high speed. A comparison with the proposed method has shown that proper settings can lead to a high degree of confidence in the frequency range of interest, while discordances arise only at higher frequencies.

Appendix A. Nomenclature

General nomenclature

L = total length of a single beam (wire) (m)

d = diameter (m)

μ = mass per unit length (kg/m)

T = constant axial load on a single beam (wire) (N)

E = Young's modulus (N/m²)

$I = \pi d^4 / 64$ = area moment of inertia (m⁴)

$K = EI$ = bending stiffness (Nm²)

w = flexural displacement (m)

$x \in [0, L]$ = spatial coordinate

x_j = position of the j^{th} intermediate support (registration arm and bracket)

J = total number of intermediate supports

x_h = position of the h^{th} connection between the wires (dropper)

H = total number of droppers

x_F = position in which a lumped non-moving force is applied to the contact wire

m_0 = equivalent lumped mass of a registration arm (kg)

m_{12} = equivalent lumped masses of a dropper, at the connections with the wires (kg)

k_0 = linear stiffness of a bracket (N/m)

k_{12} = linear stiffness of a dropper (N/m)

P = constant modulus of the moving force applied to the contact wire by the pantograph (N)

F = constant modulus of a lumped non-moving force applied to the contact wire (N)

v = constant travelling speed of the pantograph (m/s)

t = time (s)

α, β = proportional damping coefficients

FEM nomenclature

h = time step (s)

l = length of element (m)

\mathbf{v}_{n+1} = vector of displacements at time instant $t_{n+1} = h(n+1)$

$\hat{\mathbf{M}}$ = FEM mass matrix

$\hat{\mathbf{C}}$ = FEM damping matrix

$\hat{\mathbf{K}}$ = FEM stiffness matrix

$\hat{\mathbf{f}}_{n+1}$ = FEM forcing vector at time instant t_{n+1}

β = Newmark coefficient

γ = Newmark coefficient

α_m = Generalized- α method averaging coefficient

α_f = Generalized- α method averaging coefficient

ρ_∞ = Asymptotic spectral radius

References

- [1] L. Fryba, *Vibrations of solids and structures under moving loads*, Telford, London, 1999.
- [2] A. V. Metrikine, A. L. Bosch, Dynamic response of a two-level catenary to a moving load, *Journal of Sound and Vibration* 292 (2006) 676–693.
- [3] S. Y. Park, B. U. Jeon, J. M. Lee, Y. H. Cho, Measurement of low-frequency wave propagation in a railway contact wire with dispersive characteristics using wavelet transform, *Key Engineering Materials* 321–323 (2006) 1609–1615.
- [4] P. M. Belotserkovskiy, On the oscillations of infinite periodic beams subjected to a moving concentrated force, *Journal of Sound and Vibration* 193 (1996) 705–712.
- [5] T. Dahlberg, Moving force on an axially loaded beam – with applications to a railway overhead contact wire, *Vehicle System Dynamics* 44 (8) (2006) 631–644.
- [6] W. Zhang, G. Mei, X. Wu, Z. Shen, Hybrid simulation of dynamics for the pantograph–catenary system, *Vehicle System Dynamics* 38 / 6 (2002) 393–414.
- [7] J.P. Massat, J.P. Laine, A. Bobillot, Pantograph–catenary dynamics simulation, *Vehicle System Dynamics* 44 / Supplement (2006) 551–559.
- [8] L. Meirovitch, *Principles and techniques of vibrations*, Prentice Hall, New Jersey, 1999.
- [9] Y. H. Cho, Numerical simulation of the dynamic responses of railway overhead contact lines to a moving pantograph, considering a nonlinear dropper, *Journal of Sound and Vibration* 315 (2008) 433–454.
- [10] J. Ambrósio, J. Pombo, M. Pereira, P. Antunes, A. Mósca, A computational procedure for the dynamic analysis of the catenary–pantograph interaction in high-speed trains, *Journal of Theoretical and Applied Mechanics* 50 (3) (2012) 681–699.
- [11] K. J. Bathe, G. Noh, Insight into an implicit time integration scheme for structural dynamics, *Computers and Structures* 98–99 (2012) 1–6.
- [12] J. Chung, G. M. Hulbert, A time integration algorithm for structural dynamics with improved numerical dissipation: the Generalized- α Method, *Journal of Applied Mechanics* 60 (2) (1993) 371–375.
- [13] BS EN 50318:2002, Railway applications. Current collection systems. Validation of simulation of the dynamic interaction between pantograph and overhead contact line., BSI, 2002.
- [14] S. Sorrentino, S. Marchesiello, B. Piombo, A new analytical technique for vibration analysis of non-proportionally damped beams, *Journal of Sound and Vibration* 265 (2003) 765–782.
- [15] S. Sorrentino, A. Fasana, S. Marchesiello, Frequency domain analysis of continuous systems with viscous generalized damping, *Shock and Vibration* 11 (2004) 243–259.
- [16] S. Sorrentino, S. Marchesiello, B. Piombo, Analysis of non-homogeneous Timoshenko beams with generalized damping distributions, *Journal of Sound and Vibration* 304 (2007) 779–792.

- [17] G. Failla, An exact generalised function approach to frequency response analysis of beams and plane frames with the inclusion of viscoelastic damping, *Journal of Sound and Vibration* 360 (2016) 171–202.
- [18] M. Paz, W. Leigh, *Structural Dynamics: Theory and Computation*, 5th ed., Springer Science + Business media, 2004.
- [19] G. Noh, S. Ham, K. J. Bathe, Performance of an implicit time integration scheme in the analysis of wave propagations, *Computers and Structures* 123 (2013) 93-105.
- [20] M. Géradin, D. J. Rixen, *Mechanical Vibrations: Theory and Application to Structural Dynamics*, 3rd ed., John Wiley & Sons, 2015.
- [21] BS EN 50149:2001, Railway applications. Fixed installations. Electric traction. Copper and copper alloy grooved contact wires, BSI, 2001.
- [22] P. N  vik, A. R  nnquista, S. Stichel, Identification of system damping in railway catenary wire systems from full-scale measurements, *Engineering Structures* 113 (2016) 71–78
- [23] J. P. Massat, T.M.L. Nguyen Tajan, H. Maitournam, E. Balmes, Fatigue analysis of catenary contact wires for high speed trains, *9th World Congress on Railway Research (Lille, France, 22-26 may 2011)* (2011) 1-11.
- [24] S. Bruni, J. Ambrosio, A. Carnicero, Y. Hyeon Cho, L. Finner, M. Ikeda, S. Young Kwon, J. P. Massat, S. Stichel, M. Tur, W. Zhang, The results of the pantograph-catenary interaction benchmark, *Vehicle System Dynamics* 53 (3) (2015) 412-435.

Figure captions

Fig. 1. Schematic of the distributed parameter model.

Fig. 2. Definition of the test problem: non-travelling step force in a contact wire, where $L = 200$ m, $x_F = 95$ m, $x_M = 135$ m, $\mu = 1.35$ kg/m, $EI = 168$ Nm², $T = 20$ kN, $f = 100$ N.

Fig. 3. Acceleration of the measuring point x_M . Solid blue line: proposed method with proportional damping; dashed red line: Generalized- α method with no numerical damping and no structural damping; dashed-dotted green line: Generalized- α method with no numerical damping and with proportional (structural) damping.

Fig. 4. Acceleration of the measuring point x_M .

a) Solid blue line: proposed method; dashed red line: Bathe method ($l = 0.1$ m, $h = 7 \cdot 10^{-4}$ s); dashed-dotted green line: Bathe method ($l = 0.03$ m, $h = 2 \cdot 10^{-4}$ s);

b) Solid blue line: proposed method; dashed red line: Bathe method ($l = 0.08$ m, $h = 5 \cdot 10^{-4}$ s);

b) Solid blue line: proposed method; dashed red line: Generalized- α method ($\rho_\infty = 0.4$, $l = 0.08$ m, $h = 3.7 \cdot 10^{-4}$ s).

Fig. 5. Acceleration of the measuring point x_M during two time windows: before the *RTW* meets the measuring point (0.3202 s) and after the reflected *LTW* meets the measuring point (1.3610 s). Solid blue line: proposed method; dashed red line: Generalized- α method (no numerical damping); dashed-dotted green line: Bathe method.

Fig. 6. Two screenshots of the acceleration along the contact wire for the proposed method: a) $t = 0.11$ s, before the *RTW* meets the measuring point; b) $t = 0.92$ s, after the first reflection; red arrow: load point; green dot: measuring point.

Fig. 7. Acceleration of the measuring point x_M . Solid blue line: proposed method; dashed red line: Generalized- α method (no numerical damping); dashed-dotted green line: Bathe method.

Fig. 8: Definition of the test problem: moving load in a simplified overhead contact line, where $P = 200$ N, $k_{I2} = 10^5$ N/m, $k_{O2} = 10^{10}$ N/m, $v = 300$ km/h, $\mu_1 = 1.35$ kg/m, $\mu_2 = 1.07$ kg/m, $EI = 168$ Nm², $T_1 = 20$ kN, $T_2 = 16$ kN.

Fig. 9: Natural frequencies of the contact wire. a) Blue circles: proposed method; red crosses: FE method. b) Difference (%) between the two methods.

Fig. 10: Modal Assurance Criterion of the first 6 modes.

Fig. 11: Time evolution of the simplified overhead contact line model. Vertical arrows indicate the position of the load P .

Fig. 12: Results of the presented method for the measuring point $x_M = 20$ m. a) Displacement of the contact wire. b) Acceleration of the contact wire. c) Stress of the contact wire. Dashed vertical lines: time instants when the lowest speed wave meets the measuring point. Continue vertical lines: time instants when either the load or the waves reflected due to the load meet the measuring point.

Fig. 13: Acceleration of the contact wire for the measuring point $x_M = 20$ m. a) Non-zero bending stiffness $K = EI$; b) Zero bending stiffness $K = 0$.

Fig. 14: Contour plot of the total stress in the spatial-time domain. a) Stress on the messenger wire. b) Stress on the contact wire.

Fig. 15: Wave reflections related to the measuring point. Dashed arrows: time instants when the lowest speed wave meets the measuring point. Continue arrows: time instants when either the load or the waves reflected due to the load meet the measuring point.

Fig. 16: Definition of the test problem: Dynamics of a complete overhead contact line under a moving load. $P = 200$ N, $k_{l2} = 10^5$ N/m, $k_{o2} = 10^{10}$ N/m, $v = 300$ km/h, $\mu_1 = 1.35$ kg/m, $\mu_2 = 1.07$ kg/m, $EI = 168$ Nm², $T_1 = 20$ kN, $T_2 = 16$ kN, $m_0 = 0.33$ kg, $m_{l2} = 0.2$ kg.

Fig. 17: Acceleration of the contact wire at 60 m. a) Time domain - blue line: proposed method, red line: Bathe method. b) Probability distribution - blue bars: proposed method, red bars: Bathe method.

Fig. 18: Power spectral density of the acceleration of the contact wire at 60 m. a) Solid blue line: presented method; dashed red line: difference between the presented method and the Bathe method. b) Solid blue line: presented method; dashed red line: difference between the presented method and the Generalized- α method, with $\rho_\infty=1$; dashed green line: difference between the presented method and the Generalized- α method, with $\rho_\infty=0.7$; dashed yellow line: difference between the presented method and the Generalized- α method, with $\rho_\infty=0.2$.

Fig. 19: Punctual receptance of the contact wire when a harmonic load is applied at 60 m.

Fig. 20: Time evolution of the complete overhead contact line model.